Ph.D. Dissertation of Engineering

Evaluation of Ground LiDAR Derived Sky View Factor and Green View Index of Urban Streets

지상 라이다를 이용한 도시 가로 천공률과 녹시율 평가

February 2020

Graduate School of Seoul National University

Interdisciplinary Program in Landscape Architecture

Han Kyul Heo

Evaluation of Ground LiDAR Derived Sky View Factor and Green View Index of Urban Streets

Advisor: Dong Kun Lee

A dissertation submitted in partial fulfillment of the requirements for the Degree of Doctor of Philosophy in Interdisciplinary Program in Landscape Architecture in Seoul National University

February 2020

Han Kyul Heo

Approved by Thesis Committee

Chair   _____(Seal)

Vice Chair_____(Seal)

Examiner _____(Seal)

Examiner _____(Seal)

Examiner _____(Seal)

Publications

Please note that some part of this dissertation proposal was written as stand-alone papers (see below), and therefore there is some repetition in the methods and results.

1. Heo, H. K., et al., 2019, Estimating Height and Diameter at Breast Height of Urban Park and Street Trees Using Mobile LiDAR, Landscape and Ecological Engineering. 15(3), pp.253-263

2. Heo, H.K., et al., 2020. Sky View Factor Calculation in Complex Urban Geometry with Terrestrial LiDAR. Physical Geography. (Major revision)

3. Heo, H.K., et al., 2020. Human-scale Street Greenery Measurement: Improving Accuracy of Using Google Street View in Analyzing Green View Index. (Submitted)

Table of Contents

List of Figures

List of Tables

Abstract

Evaluation of Ground LiDAR Derived Sky View Factor and Green View Index of Urban Streets

Han Kyul Heo

Interdisciplinary Doctoral Program in Landscape Architecture

Graduate School, Seoul National University

Supervised by Professor Dong Kun Lee

Urban streets play an important role in improving biodiversity, storing carbon, mitigating the urban heat island effect, and on the physical and mental health of urban residents. Studies on quantifying the ecological structure of urban streets are an important research topic as they are important for urban planning. With the development of Light Detection and Ranging (LiDAR) systems, three-dimensional data acquisition is possible and an accurate ecological structure can be constructed for an urban street.

Trees are one of the most essential ecological component of urban streets and the first step is to quantifying the ecological structure of urban streets. This research used ground based LiDAR to quantify three parameters of urban trees: their height, crown base height (CBH), and diameter at breast height (DBH). The tree height and CBH, estimated by LiDAR with high

accuracy, showed a root mean square error of 0.359 m and 0.09 m, respectively, whereas the DBH was estimated with medium accuracy, showing a root mean square error of 0.0377 meters.

Sky view factor (SVF) is a key indicator to evaluate the formation of urban buildings and trees, and also used as solar energy availability index in urban heat islands and renewable energy research. A method to compute SVF in complex urban areas using LiDAR has been developed recently; however, its accuracy in areas with trees and buildings is low because of limitations in resolution of aerial LiDAR. Hence, this study tried to improve the accuracy of the SVF by using the terrestrial LiDAR and proved that using the terrestrial LiDAR provided greater accuracy than the aerial LiDAR. The results of terrestrial LiDAR-based SVF were high, with an R^2 of 0.915, RMSE of 0.037, and a maximum error of 0.156. This is more accurate than the results obtained from aerial LiDAR. This work studied whether a higher accuracy is obtainable by increasing the spatial resolution of the data. With terrestrial LiDAR, a voxel size of 2.5 is sufficient to estimate SVF in a complex urban area, reducing maximum error by 60% in comparison with aerial LiDAR, thus providing an accurate estimate.

This work explored the possibility of constructing data at a larger scale. For strategic urban planning urban-scale data that can be analyzed faster is

ideal, even at lower resolutions, but for higher efficiency. Voxelized 3D point cloud data was applied to construct a virtual environment and help researchers take advantage of using objects actually scanned by LiDAR. The result shows that lanes where the experiment was conducted significantly affected the SVF and GVI values. Therefore, through multiple simulations and computations, ideal representative points were identified which can provide the most accurate average value of the research area. Hence, when constructing urban-scale data, researchers should select an appropriate lane that best represents the average SVF and GVI of the area and thereby reduce potential error.

I. Introduction

Urban streets, a part of the urban environment, influence the biodiversity (Watts et al. 2010; Nielsen et al. 2013; Yuan et al. 2014; Pagani-Núñez et al. 2017; Canedoli et al. 2018), carbon storage (Nowak and Crane 2002; Anaya et al. 2009; Song 2013; Yoon et al. 2013; Zhao et al. 2018), urban heat island (Cao et al. 2010; Ren et al. 2013; Kim et al. 2016a; Park et al. 2017; Chun and Guldmann 2018), and physical and mental health of residents (Kim et al. 2016b; Wey and Wei 2016; Browning and Lee 2017). In particular, the influence of morphological characteristics of urban streets on public health have been highlighted in a number of studies (Odgers et al. 2012; Vanwolleghem et al. 2014; Xu et al. 2017; Chun and Guldmann 2018; Gong et al. 2018; Yu et al. 2018). These morphological characteristics such as sky view factor (SVF), green view index (GVI), building height and tree characteristics are quantified (Suzuki et al. 2001; Nowak and Crane 2002; Yoon et al. 2013; Song et al. 2016; Zhao et al. 2018; Lee and Levermore 2019) and measured directly. SVF and GVI are factors that have physical and

psychological effects, respectively (Li et al. 2015a; Bernard et al. 2018). SVF and GVI can be generated using two dimensional images such as satellite images and aerial photographs (Geiß et al. 2011; Wang et al. 2011; Li et al. 2017), however, direct measurements are incomplete and cost prohibitive, and this lack of information makes it difficult to analyze the data.

LiDAR is an active sensing method that shoots laser pulses, measures the return time of the reflected pulse, and stores the position of the object as a 3D point cloud data (Heo et al. 2019), thus collecting three-dimensional images. This data, including the information pertaining to the height of the object, makes it possible to collect urban morphological characteristics that cannot be generated by existing two-dimensional data (Chen et al. 2012; Oshio et al. 2015; Martínez-Rubio et al. 2016; Yang et al. 2016). In terms of urban street data in particular, SVF and GVI have been analyzed using photogrammetry that exhibit a low efficiency in urban-scale research. Put differently, LiDAR allows the analysis of SVF and GVI data that have been difficult to analyze without three-dimensional information.

Both SVF and GVI are important indicators of urban street environments and require three-dimensional information for analysis. SVF is an index of the relationship between the area covered by a building or tree and the degree to which the sky is visible (Souza et al. 2003; Zhang et al. 2012). SVF is mainly used for research on the urban heat island and estimation of renewable energy (Carneiro et al. 2009; An et al. 2014; Xu et al. 2017). Particularly, studies related to urban heat island mitigation and adaptation calculate the amount of radiant energy at the pedestrian level by calculating the SVF (Svensson 2004; Lindberg et al. 2008; Unger 2009). Conventional SVF data generation has been done using GIS 2.5D data or fisheye photogrammetry (Robitu et al. 2006; Lindberg et al. 2008). This method has low accuracy, and using photogrammetry it is difficult to acquire data in a large area.

GVI evaluates the number of trees visible to the human eye rather than the structure of the trees themselves. Reaching a minimum level of urban greenery has been a goal of urban planning and management (Nowak et al. 2010; Jiang et al. 2016). GVI is a measure of urban greenery and evaluates it

under human perspective that is different from the top-down view evaluation using satellite imagery or aerial photographs. GVI is calculated by the quantity of vegetation from a photograph, as interpreted by a viewer (Yang et al. 2009). Different methods, such as taking pictures from multiple directions, and using a panoramic view or 360-degree cameras, have been employed to analyze the GVI (Nordh et al. 2009; Jiang et al. 2014). Even with the development of different methodologies, it is difficult to generate data with current photogrammetry, for a scale equivalent to a city.

The accuracy of LiDAR based calculation is critical to replacing the photogrammetry method in calculating SVF and GVI. The SVF was calculated using airborne LiDAR by transforming the point cloud type data into 2.5D raster form (Carneiro et al. 2009; Susaki et al. 2014) and using the original LiDAR (Kidd and Chapman 2012; An et al. 2014). Studies relating to SVF that use highly accurate data and resolution, such as mobile LiDAR and terrestrial LiDAR, are yet to be tested. Unlike SVF, the accuracy of the mobile LiDAR derived GVI has been analyzed and it has proven to be

accurate in a certain location of small area (Susaki and Kubota 2017).

Using LiDAR data, the limitations of conventional SVF and GVI methods have can be overcome in a large scale. Nevertheless, in a larger scale analysis, analyzing all points at a high resolution requires extensive computational capacity. In this context, to ensure the possibility of constructing SVF and GVI data on a larger scale, the following two parameters are considered: 1) the reliability of the accuracy at each analysis point and 2) maintaining the accuracy of data in a large scale analysis. The main objectives of this study are to create: 1) accurate preprocessed LiDAR data for SVF and GVI data generation, 2) accurate SVF and GVI, and 3) a method for analysis at a larger scale.

II. Literature Review

1. SVF estimation

SVF is an index of the relationship between the area covered by a building or tree and the degree to which the sky is visible (Souza et al. 2003; Zhang et al. 2012). SVF is a parameter that reflects urban morphology and is highly related to the amount of solar radiation coming into the urban canopy (Watson and Johnson 1987; Hämmerle et al. 2011). For this reason, SVF is mainly used for research on urban heat islands and renewable energy estimation (Carneiro et al. 2009; An et al. 2014; Xu et al. 2017). In particular, studies related to mitigation and adaptation to the urban heat island effect have calculated the amount of radiant energy at the pedestrian level by calculating the SVF (Svensson 2004; Lindberg et al. 2008; Unger 2009).

This calculation requires a consideration of buildings and trees. The former are considered during the process of calculating SVF as they are the primary factors blocking radiant energy coming into the urban canopy (Hatefnia et al.

2017). Trees are a secondary factor in this process.

Therefore, although calculation of SVF considering trees is important it is difficult to accomplish in a complex city (Teller and Azar 2001; Teller et al. 2014). SVF is calculated by using three kinds of data: photographs and digital surface model (DSM) data in both raster format and vector format (Holmer et al. 2001; Lindberg and Grimmond 2011; An et al. 2014; Yi and Kim 2017; Gong et al. 2018). The photograph method is widely applied by using a fisheye lens that can calculate the SVF considering all elements such as trees and buildings at the pedestrian level; however, it is limited to the calculation of SVF of only one point at any given time.

To overcome this limitation, google street view image based SVF calculation technique has been developed (Gong et al. 2018; Zhang et al. 2019). This technique makes it possible to map SVF continuously by using many photographed images on the street. Despite the google street view, images taken from many different positions on the road at random lanes and constant distances needed interpolation or resulted in low-resolution mapping.

Moreover, google street view images were not taken during the same season, leading to a change in the physical appearance of trees, (Ye et al. 2018) resulting in an inaccurate SVF estimation. Therefore, continuous SVF mapping is difficult to achieve with photographs.

Alternatively, the use of GIS-based raster and vector data allows continuous SVF mapping by computing SVF for multiple points (Robitu et al. 2006; Lindberg et al. 2008). With raster data, higher resolution results in greater accuracy. Raster data stores objects in the form of a grid with a height value, so the objects are stored as a 2.5D shape. Therefore, raster data may be insufficient to reflect complicated urban structures, such as bridges and trees. Vector data can store information in 3D form, which can accurately reflect the urban structure compared to raster data. However, it is still not sufficient to store highly complex building structures and trees with great accuracy; moreover, both raster and vector data cannot be directly acquired by measuring the objects.

LiDAR (Light Detection and Ranging) can measure the structure of a city with high accuracy and has been used in urban studies to increase the accuracy of 3D structures mapping. LiDAR is an active sensor that shoots laser pulses, measures the return time of reflected pulse, and stores the position of the object as a 3D point in cloud data. Multiple studies have used airborne LiDAR to measure urban building structures (Chen et al. 2014; Yang et al. 2016), and measure the shape of trees (Hosoi and Omasa 2009; Oshio et al. 2015; Grau et al. 2017). Highly accurate LiDAR data has contributed to the increase in resolution and accuracy of the results of such studies.

Past studies have shown that SVF can be measured using LiDAR data. SVF was calculated using airborne LiDAR data to compute solar irradiance in Geneva (Carneiro et al. 2009). This study transformed the point cloud type LiDAR data into 2.5D raster form and calculated the SVF, which generated a map that was less accurate what would have been created if the original LiDAR data was applied (An et al. 2014). Research has also been done to calculate the SVF using airborne LiDAR driven 3D point cloud data (Kidd

and Chapman 2012; An et al. 2014). Studies using airborne LiDAR data directly have shown higher accuracy except for areas with trees. This is because trees have a structure made up of thin branches and small leaves, which the airborne LiDAR data is unable to express precisely.

2. GVI estimation

Reaching a minimum level of urban greenery has been a goal of urban planners and managers. Studies on street-level greenery (Yang et al. 2009), which is the degree of greenery visible to urban residents, is known to affect urban aesthetics and reduce residents' stress (Jiang et al. 2014). The concept of green view index (GVI), which derives the measure of vegetation in a photo from an individuals' perspective (Yang et al. 2009), is used to analyze street level greenery. Satellite and aerial images have been widely used to quantify the greenery affecting pedestrian or urban environments (Tan et al. 2013; Storbeck et al. 2017). However, the results from these methods differed from the actual street level greenery (Jiang et al. 2016). The most accurate

way to measure greenery at any given point is by using photogrammetry; however, it is difficult to apply to large areas.

Using images from Google Street View (GSV), Tencent street view, and Baidu street view (collectively referred to as GSV hereafter), the GVI for specific locations was estimated. GSV provides 360-degree panoramic pictures of various points in cities, which is useful to apply to GVI calculations (Li et al. 2015b; Yu et al. 2018), SVF calculations (Gong et al. 2019), street walkability (Wang et al. 2019), environment assessment of cycling routes (Vanwolleghem et al. 2014), and other analyses of the urban environment (Charreire et al. 2014; Liu et al. 2017). With the calculation of large urban-scale GVI values made possible, the relationship between GVI and environmental inequity (Li et al. 2016), physical activities (Yin and Wang 2016; Lu 2018; Lu et al. 2019; Wang et al. 2019), and housing prices (Zhang and Dong 2018) were analyzed in previous studies.

Although GSV is the most commonly used method in GVI research, LiDAR is the most accurate method. As the GSV images obtained are from

roads at a constant distance along random lanes, the results may vary

depending on camera locations.
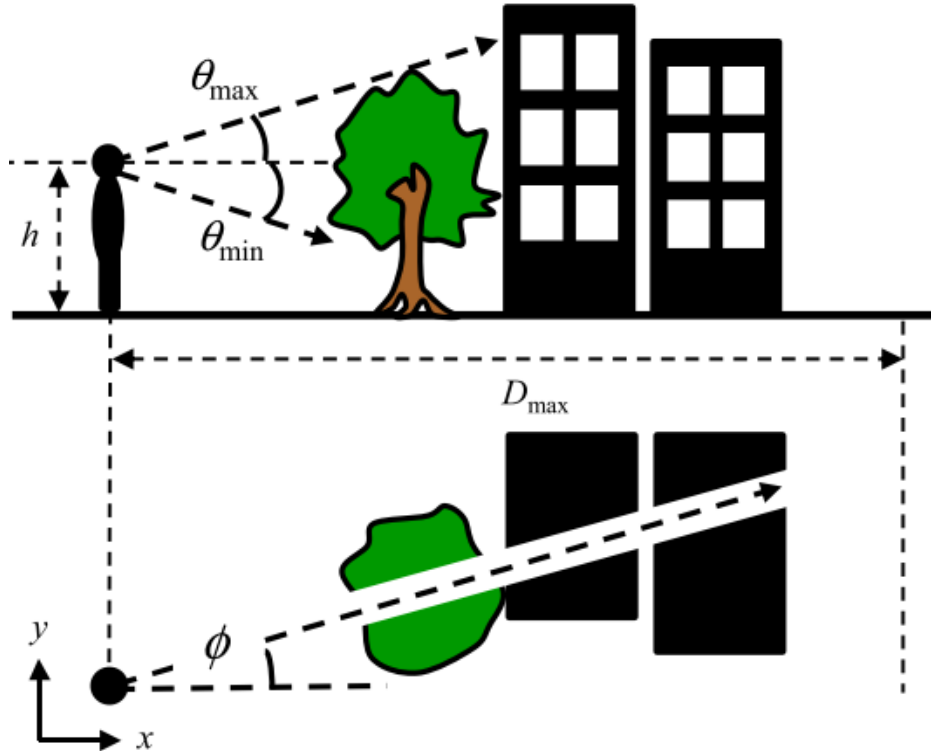
Fig. 1 Schematic of the GVI calculation process (Susaki and Kubota 2017). The GVI is calculated by considering the vertical, horizontal viewing angles at the human eye level (h). The analysis range for each analysis point is determined by designating the limit distance Dmax.

LiDAR based data method calculates the ratio of the area occluded by trees

(Susaki and Kubota 2017), which is useful for the researcher as he can

manage the angle of perception. For example, we can manage the maximum angle that a person can see and calculate GVI based on the set angle. Additionally, since the analysis point changes in multiple ways, it has the advantage of being utilized for both buildings and roads.
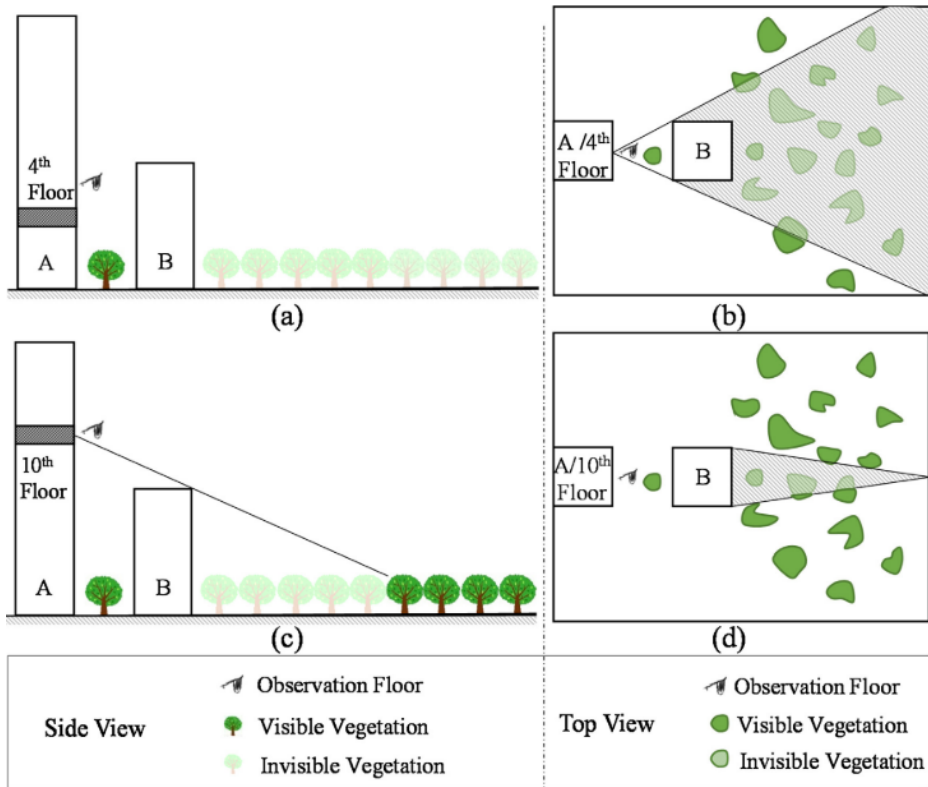
Fig. 2 Schematic image of GVI calculation process of a building (Yu et al. 2016). Based on the height of the analysis point, the object obscuring the field of view is taken into account to calculate the GVI.

In GVI analysis using LiDAR, there are studies which include the entire tree (Yu et al. 2016) and which include the green part of the tree for GVI estimation (Susaki and Kubota 2017). If the entire tree is used for GVI analysis, LiDAR data with the trees are classified is required. On the other hand, if the green part of the tree is used for GVI analysis, data is required to classify the green part of the trees. In other words, a certain level of LiDAR data preprocessing is needed to calculate GVI.

3.   Summary

Both SVF and GVI are important data, researched in urban street studies to generate LiDAR data. Airborne LiDAR studies of SVF are present, but there are no records of ground level point cloud data generation. Unlike SVF, GVI has analyzed the accuracy using point cloud data collected from mobile LiDAR; however, GVI analysis needs classified data to distinguish the green part of trees.

Table 1. Previous research about accuracy assessment and urban scale analysis with ground based LiDAR related to SVF and GVI.

	Accuracy assessment	Urban scale analysis with ground based LiDAR
SVF	X	X
GVI	O	X

GVI calculation requires preprocessing of LiDAR data. In this study, the crown of individual trees was assumed to be green. The canopy base height (CBH) was derived for crown classification. In addition, this study analyzed tree height and DBH, which are the major quantitative indicators of trees that is the major component of the urban street environment. Accordingly, the research flow was created as shown in Fig. 3.

In Chapter 3, this study investigated the preprocessing of LiDAR data for GVI calculations and accuracy of the LiDAR derived urban street tree characteristics. In Chapter 4, this study focused on the accuracy of the LiDAR derived SVF and investigated the cause of the errors. In Chapter 5, a method that does not decrease the accuracy in constructing urban scale data using LiDAR was researched.

Introduction and Literature review

Major indicators in urban street environment

Importance of the SVF in urban street environment

Importance of the GVI in urban street environment

Possibilities of LiDAR and requirements for calculating SVF and GVI

Case studies

| Chapter 3 | Evaluating the accuracy of LiDAR derived tree characteristics: tree height, DBH, CBH |
| | tree height   DBH   CBH |

| Chapter 4 | Evaluating LiDAR based SVF accuracy on complex urban street |
| | Artificial structure only   Tree only   Artificial structure and tree   Sensitivity analysis |

| Chapter 5 | Developing a method to construct urban scale data with high accuracy using LiDAR: SVF and GVI on the street |
| | **SVF** Voxel based simulation 120 settings   **GVI** Voxel based simulation 40 settings |

Conclusion

Fig. 3 Research flow

III. Evaluating the accuracy of LiDAR derived tree characteristics: tree height, CBH, DBH

1. Scope of study

In this study, tree height, CBH (crown base height), DBH (diameter at breast height) were calculated on a street and at a small urban park. The study area was selected as the area for obtaining the street tree data and the small park data. For the data acquisition of the street trees, an area located at Seoul National University, Gwanak-ro 1 Seoul, South Korea (37.57142°N, 126.9658°E) was selected (Fig. 4). It is 100 m in length and 11 m in width, including sidewalks, and there are 15 street trees on both sides (Table 2).

Table 2. Tree species on the street. A total of 15 trees of four species are planted at the study area.

Tree species	Number of trees
Ginkgo (*Ginkgo biloba*)	10
Sawleaf Zelkova (*Zelkova serrata*)	2
Prunus yedoensis (*Prunus yedoensis*)	2
Platanus (*Platanus Occidentalis*)	1

Fig. 4 Research area. View of street located at Seoul National University.

2.   Method

2.1. Mobile LiDAR and field data collection

Mobile LiDAR data from the street was collected on December 1, 2018, while field data were collected on December 3, 2018. During the field survey, specific information on urban trees, including DBH and tree height, was obtained. Point cloud data of the street was collected by a Stencil laser

scanning system, which is a stand-alone simultaneous localization and mapping (SLAM) algorithm-based real-time three-dimensional mapping device produced by Kaarta. To scan the road trees, a person carried the mobile LiDAR in the center of the road from one end of the site to the other end of the site.

This research compared tree structure quantified using the mobile LiDAR with physical measurements taken in the field. The DBH of all trees in the research area were measured with the DBH ruler. In a study using terrestrial LiDAR, the research was carried out except for trees with a DBH less than 4cm (Olofsson et al. 2014). In another study conducted in Korea, DBH of 6.2cm (Seo et al. 2015) and 4.8cm were the minimum sizes used for biomass estimation in forests and urban areas respectively (Jo and Ahn 2012; Jo et al. 2013). In this study, trees with DBH smaller than 5cm were excluded from the analysis, resulting in exclusion of 8 trees. As a result, 15 trees were measured.

2.2. Mobile LiDAR data preprocessing

Three steps of preprocessing were carried out on the mobile LiDAR data. All preprocessing steps were performed using CloudCompare software (version 2.9.1). First, noise was removed using a noise filter tool. This study applied radius 0.3, max error-relative 1.0 to option parameters. Second, ground classification was performed. This study used a CSF filter for ground classification, and the flat option was applied. Third, the trees in the study area were classified. Trees were manually classified, and tree data were segmented by individual trees. Although several automatic tree classification techniques have been developed and show high accuracy, data must be manually postclassified due to incomplete classification (Zhao et al. 2018). Therefore, this research manually classified and segmented the trees.

2.3. Tree height estimation

This research calculated the tree height using the height-above-ground method. The height above ground was calculated by subtracting the height value of the point from the height value of the ground surface. For each individual tree point cloud, the maximum value of the height above ground was taken as the tree height. The height-above-ground calculation was performed using the cloud/mesh distance tool in CloudCompare software, and the maximum height-above-ground value of each tree was computed using MATLAB 2018b.

2.4. CBH estimation

For each individual tree point cloud data was used to estimate CBH. CBH can be calculated by measuring the distance from the ground to the lowest branch of the tree crown (Næsset and Økland 2002; Popescu and Zhao 2008; Luo et al. 2018). In this research, CBH for verification was manually

measured by extracting the lowest point among the tree crown points (Jung et al. 2011).

To calculate CBH, the point cloud data of the tree was extracted in 10cm interval from the ground parallel to the x, y plane. For each slice, convex hull using x, y coordinates was derived, and the side length of the convex hull was calculated. As a result, the side length data of the convex hull was constructed every 10 cm of the 15 trees. As the height increase, side length data will highly increase when the crown. That is, CBH can be determined based on the increment of the side length. To determine the threshold increment, this research tested threshold values including 10cm, 15cm, 20cm, 25cm, 30cm.

2.5. DBH estimation

DBH refers to the diameter of a tree trunk measured at a height of 1.2 m. Mobile LiDAR scanned data have a lower point density than terrestrial LiDAR. Therefore, the shape of the trunk cannot be extracted when extracting

data only at a height of 1.2 m. In this study, DBH was calculated for each tree

by extracting scanned points from 1.19 m - 1.21 m height from the ground.
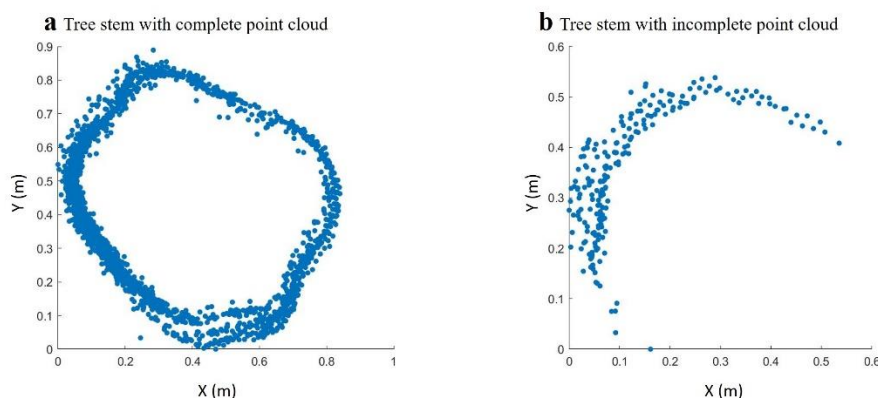
Fig. 5 Point cloud data acquired at breast height (1.19-1.21m above the ground). a Point cloud data with full point coverage around the trunk. b Point cloud data with half point coverage around the trunk.

Many studies have been carried out to measure the DBH of trees using

terrestrial LiDAR (Côté et al. 2011; Huang et al. 2011; Yao et al. 2011).

However, the mobile LiDAR data used in this study have incomplete

information on the tree trunk because full point coverage around the trunk

could not be obtained for some trees (Fig. 5b). That is, this study needed a

method that estimated the remaining part by using incomplete data. Therefore,

this research employed the least-squares circle fitting method in this study

(Pratt 1987).

2.6. Statistical analysis

Statistical analysis was performed to evaluate the accuracy of tree height and DBH. The accuracy of the results was verified by calculating the correlation coefficient (R2) and root mean square error (RMSE). R2 is computed as follows:

$$R^2 = 1 - \frac{\sum_{i=1}^{n}(E_i - M_i)^2}{\sum_{i=1}^{n}(E_i - M_{imean})^2}$$

where n is the number of trees, E_i and M_i represent the estimated and measured values, respectively, and M_{imean} is the average of the measured values. RMSE was computed as follows:

$$RMSE = \left(\frac{1}{n}\sum_{i=1}^{n}(E_i - M_i)^2\right)^{\frac{1}{2}}$$

The higher the R2 and the lower the RMSE, the higher the accuracy. R2 and RMSE were calculated for each study site and calculated for DBH and for tree height.

3. Result

3.1. LiDAR data construction
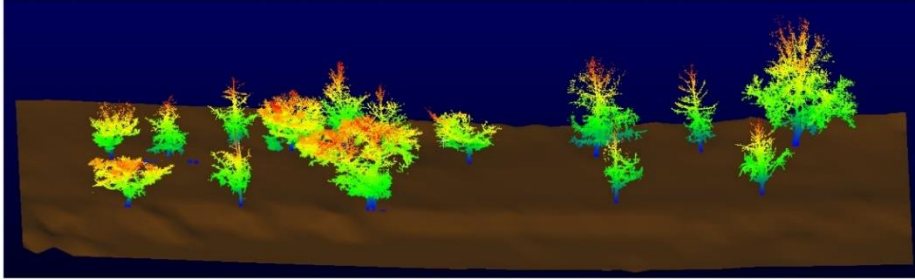
Fig. 6 Collected mobile LiDAR data with preprocessing performed. Each tree is a separate object colorized by the height above ground value. Ground points were replaced by ground mesh. (a) Data collected at the road.

Fig. 6 shows the collected mobile LiDAR data that preprocessing was performed on. A small number of points were created at the top of the tree compared to the bottom. This is because the mobile LiDAR has a low vertical field of view (FOV) of 30, and lasers were blocked by the surrounding tree crowns.

3.2. Tree height estimation

This research first computed the tree heights extracted from the height above ground value. To assess accuracy, the estimated tree heights were compared to the measured tree heights (Table 3). The difference between the measured and estimated heights had a mean value of 0.24 m, and the maximum error was 0.8 m.

Table 3. Field-measured and LiDAR-estimated heights of trees. The maximum height difference was shown at r-3. Most tree heights were underestimated.

Tree (ID)	Measured Height (m)	Estimated Height (m)	Height Difference (m)	Tree (ID)	Measured Height (m)	Estimated Height (m)	Height Difference (m)
r-1	7.5	7.6	-0.1	r-9	12.4	12.1	0.3
r-2	9.7	9.5	0.2	r-10	16.6	16.5	0.1
r-3	11.0	10.2	0.8	r-11	6.4	6.6	-0.2
r-4	7.8	7.6	0.2	r-12	9.1	9.0	0.1
r-5	11.9	11.7	0.2	r-13	10.5	10.4	0.1
r-6	10.8	10.4	0.4	r-14	11.6	10.9	0.7
r-7	8.7	8.5	0.2	r-15	11.3	10.8	0.5
r-8	13.8	13.5	0.3				

3.3. CBH estimation

This study estimated the CBH from the individual tree point cloud data. The convex hull length was calculated to derive the CBH (Appendix 1, Appendix 2). To assess the accuracy, manually extracted CBHs were compared to the measured tree heights (Table 4). The difference between the manually extracted and estimated heights had a mean value of 0.09 m, and the maximum error was 0.3 m. Based on the CBH, this research could classify trunk and crown of the trees (Fig. 7, Fig. 8).

Table 4. Manually extracted and estimated CBH of trees. The maximum difference was shown at r-11.

Tree (ID)	Manually extracted CBH (m)	Estimated CBH (m)	Height Difference (m)	Tree (ID)	Manually extracted CBH (m)	Estimated CBH (m)	Height Difference (m)
r-1	1.28	1.2	0.08	r-9	1.41	1.5	-0.09
r-2	0.74	0.7	0.04	r-10	2.26	2.2	0.06
r-3	1.41	1.3	0.11	r-11	1.47	1.7	-0.23
r-4	1.22	1.3	-0.08	r-12	1.66	1.6	0.06
r-5	1.92	1.9	0.02	r-13	2.15	2.2	-0.05
r-6	2.68	2.8	-0.12	r-14	1.50	1.8	-0.30
r-7	1.78	1.8	-0.02	r-15	1.51	1.6	-0.09
r-8	1.50	1.4	0.10				
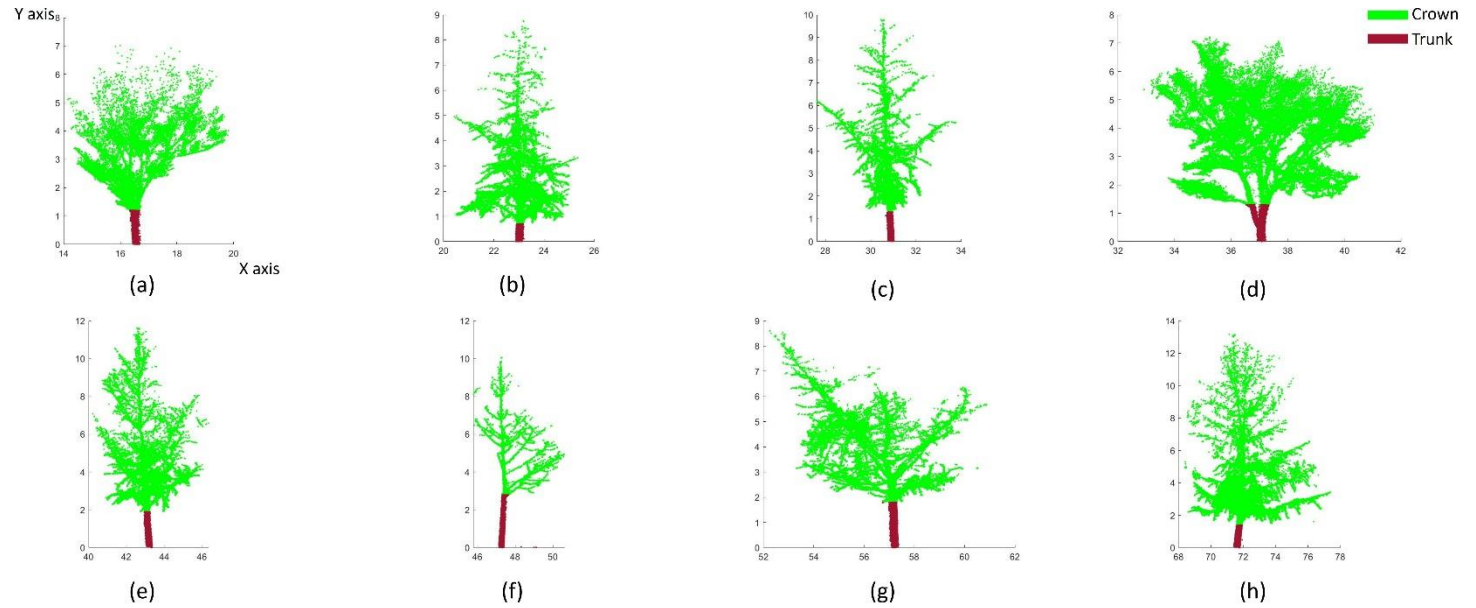
Fig. 7 Crown classified trees based on CBH (r1-r8). Green represents the crown of the tree and brown represents the trunk of the tree.
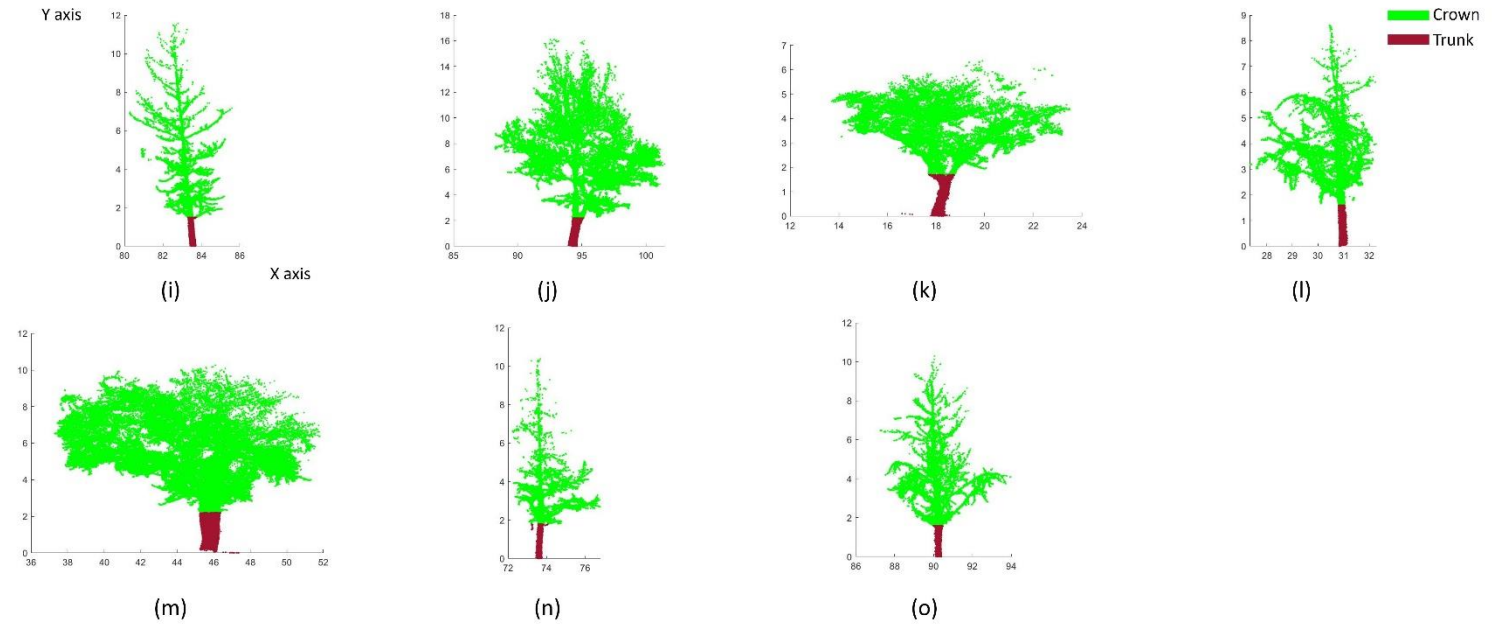
Fig. 8 Crown classified trees based on CBH (r9-r15). Green represents the crown of the tree and brown represents the trunk of the tree.

3.4. DBH estimation

This research computed the DBH extracted from the point cloud at 1.19 m-1.21 m. Unlike tree height, DBH does not calculate only one value per tree because there are some trees whose trunk splits less than 1.2 m from the ground. This study measured and estimated the DBH of those trees.

Table 5. Field-measured and LiDAR-estimated DBH. The maximum DBH difference was shown at r-13. Most tree heights were overestimated.

Tree (ID)	Measured DBH (cm)	Estimated DBH (cm)	DBH Difference (cm)	Tree (ID)	Measured DBH (cm)	Estimated DBH (cm)	DBH Difference (cm)
r-1	19.6	20.5	-0.9	r-8	30.2	29.8	0.4
r-2	21.4	23.0	-1.6	r-9	22.1	22.3	-0.2
r-3	18.6	21.1	-2.5	r-10	51.9	54.4	-2.5
r-4-a	11.9	16.0	-4.1	r-11	32.3	36.0	-3.7
r-4-b	13.2	20.6	-7.4	r-12	19.4	22.3	-2.9
r-4-c	10.5	16.7	-6.2	r-13	73.0	80.7	-7.7
r-5	23.6	27.9	-4.3	r-14	21.8	21.8	0.0
r-6	17.5	21.6	-4.1	r-15	22.1	22.1	0.0
r-7	23.5	23.3	0.2				

To assess accuracy, the estimated DBH values were compared to the measured DBH values (Table 5). The difference between the measured and estimated heights had a mean value of -2.79 cm, and the maximum error was -7.7 cm.

3.5. Statistical analysis

This study also evaluated the accuracy by calculating the root mean square error (RMSE) and the correlation coefficient. Concerning tree height, as shown in Fig. 4, the correlation coefficient was 0.963 with an R square of 0.988 and the RMSE was 0.359 m, which indicated that there was a high correlation between the measured and estimated tree heights.
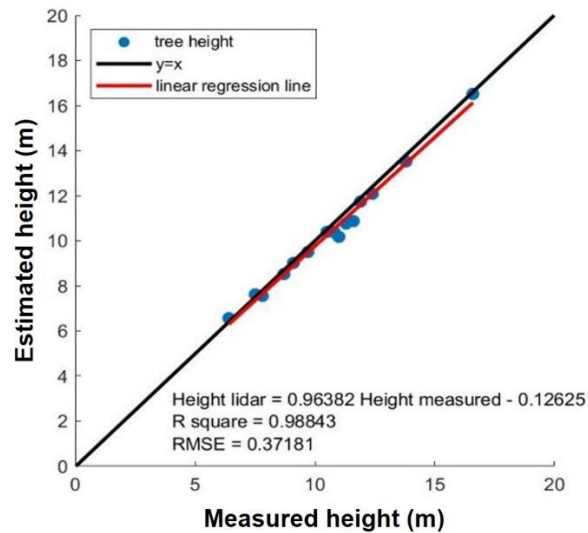
Fig. 9 Scatter plot, linear regression line and ideal line between the measured tree height and estimated tree height using mobile LiDAR. Most points are distributed near the ideal line. The linear regression line appears similar to the ideal line.

Concerning CBH, as shown in Fig. 11, the correlation coefficient was

0.9214 with an R square of 0.937 and the RMSE was 0.12 m. The manually

extracted and estimated CBH has high correlation. However, compared to tree

height estimation, CBH has relatively high RMSE.
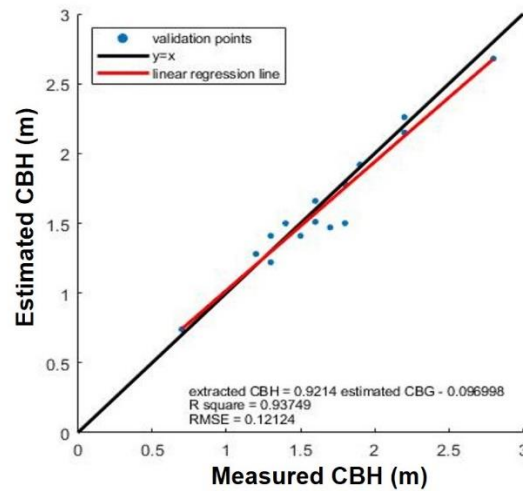
Fig. 10 Scatter plot, linear regression line and ideal line between the manually extracted CBH and estimated CBH using mobile LiDAR. Most points are distributed near the ideal line, but are more dispersed than the tree height. The linear regression line appears similar to the ideal line.

Concerning DBH, as shown in Fig. 11, the correlation coefficient was

1.033 with an R square of 0.973 and the RMSE was 3.77 cm. The measured

and estimated DBH has high correlation. However, compared to tree height

estimation, there was a relatively low correlation between the measured and
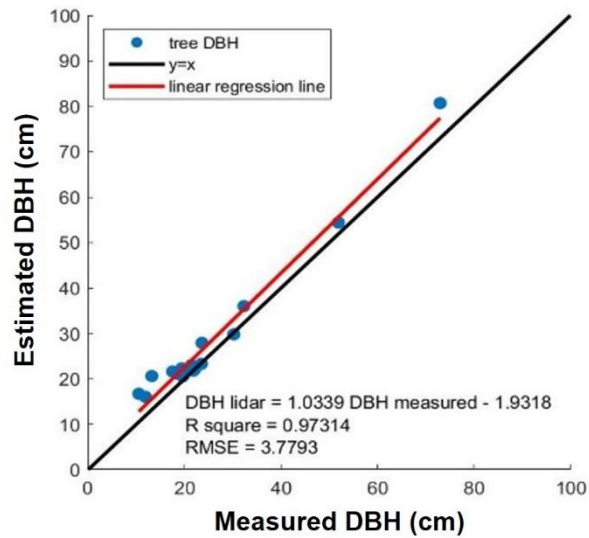
estimated DBH.

Fig. 11 Scatter plot, linear regression line and ideal line between the measured DBH and estimated DBH using mobile LiDAR. Most points are distributed near the ideal line and slightly overestimated, but are more dispersed than the tree height.

4. Discussion

This study calculated tree height, CBH, DBH of trees using mobile LiDAR

and evaluated its accuracy by comparing it with field-based measurements.

Unlike terrestrial LiDAR, mobile LiDAR can scan a large area, which could

enable the construction of data at the city level. This study evaluates the potential accuracy of that scaling up of data. According to the result, it is possible to calculate tree height, CBH and DBH for the street trees in urban areas using mobile LiDAR with a high degree of accuracy.

Mobile LiDAR has other advantages in addition to being able to measure large areas when compared to terrestrial LiDAR. Unlike LiDAR measurements in a forest, measurements in urban areas are more challenging due to the difficulty of controlling the measurement situation. Obstacles in urban areas result in shadows, which are areas with no data (Bonnaffe et al. 2007). Cars passing by or parked on the street can block tree trunks and people on the street or at the park may also block trees. In this case, terrestrial LiDAR scanning from certain points results in shadows, whereas mobile LiDAR moves while scanning, thus the trees are not completely hidden. Nonetheless, these obstacles lower the density of the point cloud and reduce the accuracy of the final estimation.

There were factors that decreased the estimation accuracy. The estimated

tree heights were generally slightly underestimated compared to the measured tree heights (Fig. 9). As the average height difference indicates, the estimated tree heights were lower than the measured tree heights in the study areas. The differences between the measured and estimated tree heights were larger when the tree heights were higher. The underestimation is likely related to the low point density at the top of the trees in mobile LiDAR data. Because mobile LiDAR has a smaller vertical FOV, the upper part of the tree can only be scanned far from the tree, which results in a lower point density. The low point density at the top of the tree indicates that the mobile LiDAR is unlikely to scan the highest part of the tree. For instance, (Hopkinson et al. 2004) calculated tree height from ground-based LiDAR data and underestimated the height due to foliage obstruction, particularly for tall trees. Unlike tall trees, small trees have relatively high accuracy because mobile LiDAR scans are less likely to be blocked by the tree crowns.

CBH is used to estimated by using airborne LiDAR and density of the point cloud data (Popescu and Zhao 2008). Point cloud data of the tree crown

with frequency and intensity crown vertical profiles were used because airborne LiDAR cannot evenly scan whole tree structure. However, terrestrial and mobile LiDAR can evenly scan the tree so that vertical profile cannot be applied (Jung et al. 2011). Therefore, this research applied morphological features of trees to estimate CBH.

The estimated DBH was generally slightly overestimated compared to the measured DBH (Fig. 11). As the average DBH difference indicates, the estimated DBHs were generally larger than the measured DBHs in both study areas. The irregular shape of tree trunks and incomplete point data around the trunk are likely the reasons (Fig. 12c). DBH can be estimated with higher accuracy when the tree has a circular trunk (Yao et al. 2011; Fan et al. 2018). Contrary to (Fan et al. 2018), the result of this study was biased because tree stems in this study do not form a uniform circular shape.
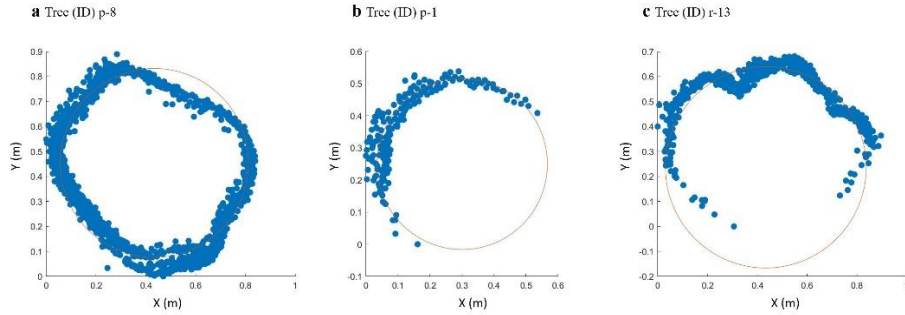
Fig. 12 Points at breast height and their fitted circles: a. complete point coverage with precise trunk shape, b. incomplete point coverage, c. incomplete point coverage around the trunk and the irregular shape of the trunk.

Since the DBH estimation has a large error compared to the tree height estimation, this study explored the reasons for the error. There were two major factors that decreased DBH estimation accuracy. One source of error was the relatively low precision of the mobile LiDAR-driven point cloud data. Because the mobile LiDAR scanned data have lower precision than terrestrial LiDAR (Pierzchała et al. 2018), it is difficult to detect precise trunk shapes (Fig. 12a). Another source of error was the combined effect of incomplete point coverage around the trunk and the irregular shape of the trunk (Fig. 12c). Although tree p-1 has incomplete point coverage (Fig. 12b), there is a small difference between the measured and estimated DBH. However, as shown in

Fig. 12c, tree DBH is overestimated when the data are incomplete and the shape is irregular.

Tree height, CBH, DBH are basic structure parameters for quantifying tree characteristics (Huang et al. 2011; Jung et al. 2011; Song and Ryu 2015; Luo et al. 2018). Tree height and DBH have been used as variables to calculate carbon storage of individual tree (Nowak and Crane 2002; Yoon et al. 2013; Zhao et al. 2018). CBH have been used for measuring crown volume (Korhonen et al. 2013) and tree health monitoring (Korhonen et al. 2013). Thus, the vertical structure and horizontal pattern effect of green space is quantified, and the width of tree is measured by using satellite image or the aerial photograph. However, since tree height, DBH and CBH were difficult to compute from satellite images, field survey has been done (Yoon et al. 2013; Seo et al. 2015; Song and Ryu 2015). Therefore, acquiring data from each individual tree is time-consuming and laborious. According to this research, LiDAR can be used to measure the DBH and tree height, making it possible to overcome the inefficiency of direct irradiation.

IV.   Evaluating LiDAR based SVF accuracy on

complex urban street

1.   Scope of study

This study tried to calculate the SVF, beginning from an indoor area with simple conditions, extending to complex outdoor conditions, and a Terrestrial LiDAR was employed to collect urban geometry data, and a fisheye lens photo to verify the results.
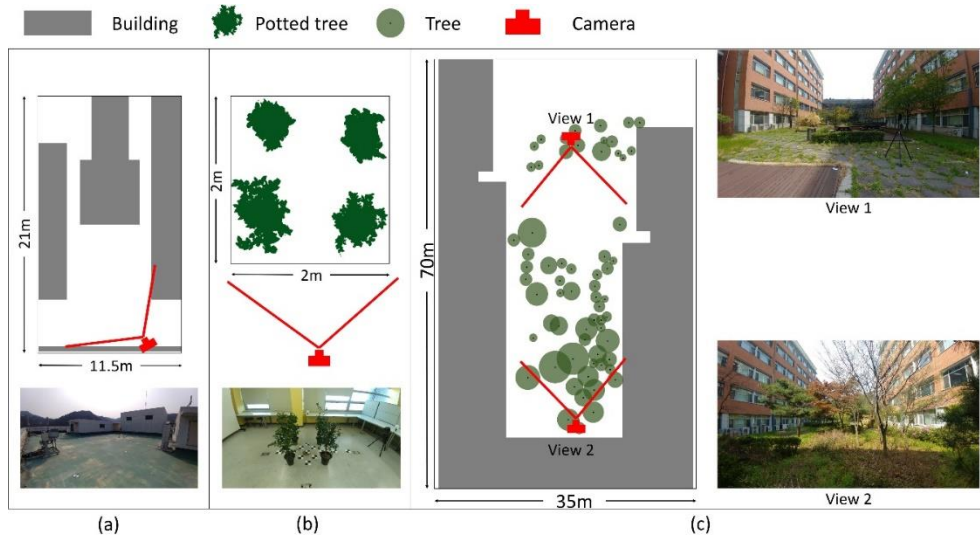
Fig. 13 Research area: (a) Testbed A (artificial structure), (b) Testbed B (vegetation), (c) Testbed C (actual complex structure).

Artificial structures such as buildings and natural occurrences such as trees are two main sources that affect SVF in urban areas. Therefore, this study selected testbeds with three different conditions to calculate the SVF and evaluate its accuracy. Two testbeds with stable conditions, having zero effect of wind on their main obstacles, will not result in a SVF calculation error. In consideration of the buildings in the city, Testbed A consisted of artificial structures only. as it is difficult to find an area with only buildings, this research selected the roofs of some buildings for this. They had a low to high SVF due to narrow pathways and open spaces (Fig. 13a). In consideration of the trees and plants in the city, testbed B had consisted of vegetation only. To study this condition, four potted trees were set up in a room at 2×2 m rectangular vertices (Fig. 13b). The minimum tree height was 1.2 m and maximum was 1.3 m; these included a pot height of 0.25 m.

Testbed C has a complex outdoor structure with buildings and vegetation (Fig. 13c). This research selects this testbed to confirm the possibility of SVF computation method using terrestrial LiDAR in a complex city. The left- and

right-hand side buildings were six stories high; on the down side was a three-story building. There was a garden between the buildings with various trees planted in it. The entrance area is dense with trees and the interior is relatively open. Given that buildings surround the area from three directions and the fourth is left open, the lower area of the building is influenced by SVF, which this decreases as the analysis points goes up. As the trees are unevenly distributed, the effect of their diversity is captured in testbed C. Additionally, this study set up a testbed D that was similar to testbed C by removing the collected data of buildings. All testbeds were located at Seoul National University, Seoul, South Korea.

2. Method

2.1. Terrestrial LiDAR data collection

Scanning of selected research areas was done between March and April 2018 with a FARO Focus3D-S350 instrument. Scanning was conducted to minimize the shaded area with resolution at a point spacing of 4 mm at 25 m

distance and up to 966,000 points per second. Details pertaining to the scanning conditions are as shown in Table 6. This research registered the scanned data with the registration tool of the software Faro Scene 7.1. Each registered testbed was sliced with a cross-section tool of the software CloudCompare to extract the region of interest.

Table 6. Terrestrial LiDAR and fisheye lens photo observation specifications at each testbed.

		Testbed A	Testbed B	Testbed C
LiDAR	Number of scanning positions	9	14	23
	Number of targets	44	12	39
	Date	March 13, 2018	March 16, 2018	April 26, 2018
Fisheye image	Height above the target	50 cm	50 cm	100 cm
	Number of pictures	44	12	39
	Date	March 13, 2018	March 16, 2018	April 26, 2018

2.2. SVF calculation with terrestrial LiDAR (SVFt)

Original 3D point cloud data acquired from terrestrial LiDAR was voxelized to compute the SVF. Voxel is a compound word combining volume and pixel, meaning a pixel having a volume. Point cloud data are not suitable for representing the surface of an object because it is data with an empty space between points. To compensate this drawback, this study used the data as a voxel. Additionally, the redundant point cloud data is eliminated by voxelizing it, thus reducing the size of the data and shortening the computing time. This study did not apply vertical offset because of the characteristics of terrestrial LiDAR. It is selectively applied when calculating SVF with 3d point cloud data (An et al. 2014). Data is classified in consideration of the characteristics of the obstacle, and vertical offset is not applied in case the obstacle, such as a tree or bridge, had an empty bottom. This is because the airborne LiDAR allows easy detection of the top of an object beneath it, but difficult to detect the object's bottom. Therefore, a classification process of the LiDAR data was not conducted.

A ray-tracing algorithm was applied to compute SVF (Souza et al. 2003).

First, this study checked the objects that covered the sky at every calculation

point. Hypothetical rays representing the same solid angle were shot out from

the calculation point to the sky covering that hemisphere. Rays were divided

as those making or not making contact with the object voxel. Secondly, based

on the horizontal and vertical angle of the rays, SVFt was computed as

follows:

$$SVFt = \left(1 - \frac{\sum_{r=1}^{m} sin\gamma_r}{\sum_{i=1}^{n} sin\gamma_i}\right)$$

where n is the number of rays in the computation process; i the ith ray;

γ_i the vertical angle of the ray i. The computation was conducted using

MATLAB R2017a.

In the SVF calculation using ray tracing, the size of the voxel and spacing

between the rays are related to the accuracy of results. If the LiDAR data has

a sufficient number of points, the smaller the voxel size, the higher the

accuracy of the surrounding environment. However, accuracy of the

surrounding environment decreases if the LiDAR data has a small number of points, and there is an empty space inside the object when the voxel size is small. Ray interval is also related to the detection of nearby objects to calculate SVF. The smaller the ray interval, the more precise is the detection of the shape of the object. Therefore, with smaller space between rays, SVF can be calculated with higher accuracy.

Therefore, this study calculated SVF with different voxel sizes and ray intervals at testbeds A and B, respectively. Because these two testbeds have a simplified condition, this study could analyze the effect of voxel size and ray intervals on each artificial structure and trees. Voxel size of 20, 10, 5 and 2.5 cm were analyzed with ray interval of 0.5 degree, and Ray interval of 1, 0.5, 0.25 degrees were analyzed with a voxel size of 2.5 cm.

A continuous SVF map was constructed for each testbed, and to evaluate accuracy, the SVF above the targets was calculated at a specific height. SVF was calculated at 50 cm, above the targets in testbed A and B and at 100 cm above testbed C. The condition of the SVFt calculation is listed in Table 7.

Table 7. SVFt calculation conditions in each testbed.

	Testbed A	Testbed B	Testbed C
Voxel size	5 cm	2.5 cm	5 cm
Ray interval	0.5°	0.5°	1°
Heights above the target	50 cm	50 cm	100 cm

2.3. SVF calculation with a fisheye lens (SVFf)

To verify the SVF calculation method with terrestrial LiDAR data, SVF was measured using a fisheye lens as reference. In this study, fisheye photographs were captured using a Nikon D810 camera with SIGMA 8 mm F3.5 circular fisheye lens. Fisheye images were taken above the target at different heights depending on the condition of the testbeds (Table 7). A camera was mounted on a tripod to achieve sufficient height.

The SVF calculation with a fisheye lens was performed using the SOLWEIG SVF calculator (Lindberg et al. 2008). This calculator is one of the SOLWEIG-models from the University of Gothenburg and can calculate SVF from fisheye images.

2.4. Accuracy analysis

Verification points were selected at positions where fisheye-lens images were taken, and SVFt was calculated at the same positions. The accuracy of the model was verified by calculating the root mean square error (RMSE) and correlation coefficient (R2) of the findings. The RMSE is computed as follows:

$$\text{RMSE} = \left(\frac{1}{n} \sum_{i=1}^{n} (T_i - F_i)^2 \right)^{\frac{1}{2}}$$

where T_i is the computed SVFt, F_i is the SVFf, and n is the number of verification points. R2 is computed as follows:

$$R^2 = 1 - \frac{\sum_{i=1}^{n}(T_i - F_i)^2}{\sum_{i=1}^{n}(T_i - F_{imean})^2}$$

where n is the number of verification points; T_i and F_i represent the computed SVFt and SVFf, respectively; and F_{imean} is the average of the computed SVFf.

2.5. Tree effect on SVF calculation

In order to investigate the effect of trees on SVF calculations, a testbed D was setup similar to testbed C but without the data of buildings. At first, this study removed data pertaining to buildings from terrestrial LiDAR data and fisheye lens photographs. Secondly, SVFt and SVFf were calculated using that data. Removal of data pertaining to buildings in terrestrial LiDAR data was done using the interactive segmentation tool of the software CloudCompare. Fuzzy selection, select by color, and the eraser tools of in the software GIMP were applied to remove the data of buildings from the fisheye lens photographs. With this data, this research calculated SVFt and SVFf and compared the results and accuracy of terrestrial LiDAR based SVF, analyzed in the testbeds C and D.

2.6. Sensitivity analysis

The voxelization process assigns a volume to a point that has no volume. In this process, the size of the object is overestimated. Additionally, even if

the same sized voxel is used, the possibility of being found by the ray varies according to the position of the voxel and its distance from the measurement point. When the size of the voxel is small or it is far from the measurement point, the voxel is less likely to be found by the ray. One way to compensate for this is to narrow the ray interval.

To analyze how voxel size and ray interval affects SVF, sensitivity analysis was performed, and Voxelized points were randomly generated at a distance of 1 m and 20 m from the analysis point. This research analyzed how the generated voxel affects SVF depending on different ray intervals. Voxel sizes of 5, 10, and 20 cm and ray intervals of 0.5°, 1°, 2°, 4° and 8° were simulated (Table 8). This process was repeated 100,000 times.

Table 8. Simulation variables and values. Voxel size and ray interval are the main component of the sensitivity analysis. Both voxel size and ray interval were doubled from baseline.

Voxel size	5 cm	10 cm	20 cm
Ray interval	0.5°, 1°, 2°, 4°, 8°	0.5°, 1°, 2°, 4°, 8°	0.5°, 1°, 2°, 4°, 8°

3. Result

3.1. LiDAR data construction

Fig. 14 shows point cloud data at each testbed. Scanning was conducted at 9, 14, and 23 positions in testbeds A, B, and C, respectively. Testbed A covers a 20 m × 42 m square area consisting of 257,669,139 points and a maximum structure height of 9.8 m. Testbed B covers a 2 m × 2 m square area consisting of 9,039,101 points and a maximum tree height of 1.3 m and Testbed C covers a 24 m × 69 m square area, consisting of 439,985,137 points and a maximum structure height of 29.9 m (Table 9).

Table 9. Basic information of terrestrial LiDAR data at each testbed.

	Testbed A	Testbed B	Testbed C
Covered area	20 m x 42 m	2 m x 2 m	24 m x 69 m
Number of points	257,669,139	9,039,101	439,985,137
Maximum height	9.8 m	1.3 m	29.9 m
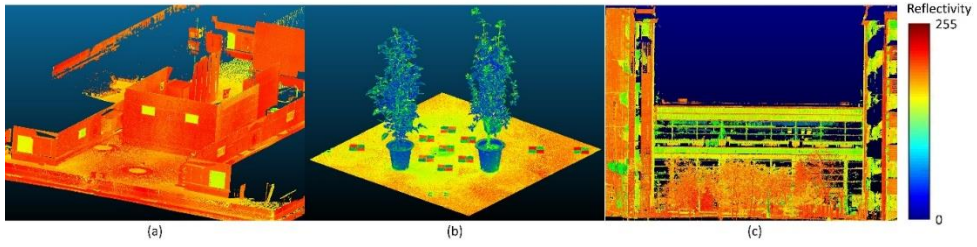
Fig. 14 Collected LiDAR data: (a) Testbed A, (b) Testbed B, (c) Testbed C. Color represents the reflectivity at the captured surface. In general, bright surfaces have higher reflectivity than dark surfaces.

3.2. Testbed A

In testbed A, SVF was calculated using 44 fisheye photographs and terrestrial LiDAR at the same points (Table 10). The SVF error at testbed A has mean, maximum and minimum values of 0.038, 0.088, and 0.002, respectively. SVF errors of 95% or more showed an error range less than 0.7. A high R2 (0.984) and a low RMSE (0.0432) value indicate that the SVFt is extremely close to the SVFf.

Table 10. Computed SVF and difference between SVFt and SVFf in testbed A.

Point (ID)	SVFt (T)	SVFf (F)	SVF Difference (T)-(F)	Point (ID)	SVFt (T)	SVFf (F)	SVF Difference (T)-(F)
1	0.467	0.440	0.027	23	0.726	0.728	-0.002
2	0.449	0.440	0.009	24	0.874	0.905	-0.031
3	0.448	0.390	0.058	25	0.942	0.989	-0.047
4	0.430	0.384	0.046	26	0.958	0.996	-0.038
5	0.354	0.294	0.060	27	0.950	0.995	-0.045
6	0.098	0.162	-0.064	28	0.950	0.995	-0.045
7	0.346	0.434	-0.088	29	0.832	0.848	-0.016
8	0.685	0.683	0.002	30	0.882	0.896	-0.014
9	0.722	0.720	0.002	31	0.958	0.991	-0.033
10	0.696	0.715	-0.019	32	0.971	1.000	-0.029
11	0.612	0.540	0.072	33	0.970	1.000	-0.030
12	0.771	0.808	-0.037	34	0.955	0.989	-0.034
13	0.843	0.897	-0.054	35	0.952	0.996	-0.044
14	0.824	0.871	-0.047	36	0.935	0.985	-0.050
15	0.870	0.922	-0.052	37	0.505	0.474	0.031
16	0.861	0.913	-0.052	38	0.412	0.350	0.062
17	0.772	0.812	-0.040	39	0.147	0.166	-0.019
18	0.869	0.913	-0.044	40	0.046	0.067	-0.021
19	0.925	0.978	-0.053	41	0.109	0.168	-0.059
20	0.926	0.980	-0.054	42	0.442	0.398	0.044
21	0.904	0.960	-0.056	43	0.531	0.536	-0.005
22	0.820	0.835	-0.015	44	0.396	0.438	-0.042

3.3. Testbed B

In testbed B, SVF was calculated using 12 fisheye photographs and terrestrial LiDAR at the same points (Table 11). The SVF error at testbed A has a mean, maximum, and minimum value of 0.033, 0.086, and 0.005, respectively. SVF errors were all less than 0.04, indicating that the accuracy

was high. A high R2 (0.819) and low RMSE (0.04) value indicate that the

SVFt is close to SVFf.

Table 11. Computed SVF and difference between SVFt and SVFf in testbed B.

Point (ID)	SVFt (T)	SVFf (F)	SVF Difference (T)-(F)	Point (ID)	SVFt (T)	SVFf (F)	SVF Difference (T)-(F)
1	0.971	0.966	0.005	7	0.819	0.780	0.039
2	0.895	0.872	0.023	8	0.806	0.784	0.022
3	0.725	0.759	-0.034	9	0.695	0.727	-0.032
4	0.668	0.744	-0.076	10	0.759	0.730	0.029
5	0.716	0.737	-0.021	11	0.654	0.741	-0.087
6	0.748	0.760	-0.012	12	0.888	0.867	0.021

3.4. Testbed C

SVF map was derived in testbed C with 0.5 m resolution. The cross-

sectional map and SVF graphs are compared at three points. Buildings and

trees are the two main sources that decrease the SVF. Because the buildings

are located at both ends, SVF decreased significantly at both ends (Fig. 15b,

c, d). Graphs were fluctuated according to tree position. As shown in Fig. 15c,

relatively big trees were evenly planted which resulted in the appearance of

zero in the middle of the research area. In contrast, there were relatively small

trees resulting in values greater than zero, as shown in Fig. 15b. In Fig. 15d,

because four trees are clustered to the right, the SVF value converged to zero.
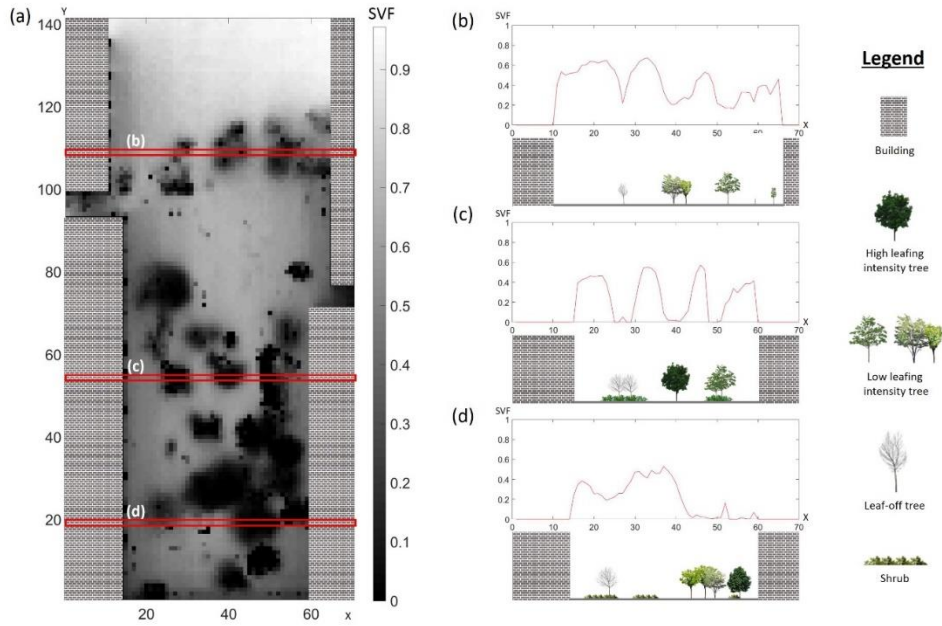
Fig. 15 SVF map of testbed C. (a) A SVF map of testbed C with a resolution of 0.5m, (b) SVF graph and cross-section map at Y axis 108, (c) SVF graph and cross-section map at Y axis 57, (d) SVF graph and cross-section map at Y axis 20. The x axis of (b), (c), (d) is the same as (a), and the y-axis represents the SVF value.

In testbed C, SVF was calculated using 39 fisheye photographs and

terrestrial LiDAR at the same points (Table 12). The SVF error at testbed A

has a mean, maximum, and minimum values of 0.022, 0.153 and 0. SVF

errors of 90% or more showed an error range of less than 0.1. A high R2

(0.915) and low RMSE (0.037) value indicates that the SVFt is close to SVFf.

Table 12. Computed SVF and difference between SVFt and SVFf in testbed D.

Point (ID)	SVFt (T)	SVFf (F)	SVF Difference (T)-(F)	Point (ID)	SVFt (T)	SVFf (F)	SVF Difference (T)-(F)
1	0.489	0.509	-0.02	21	0.639	0.627	0.012
2	0.519	0.526	-0.007	22	0.681	0.677	0.004
3	0.243	0.349	-0.106	23	0.696	0.679	0.017
4	0.538	0.593	-0.055	24	0.699	0.707	-0.008
5	0.612	0.613	-0.001	25	0.703	0.686	0.017
6	0.630	0.617	0.013	26	0.708	0.697	0.011
7	0.573	0.573	0.000	27	0.689	0.695	-0.006
8	0.626	0.620	0.006	28	0.690	0.667	0.023
9	0.629	0.606	0.023	29	0.676	0.656	0.020
10	0.444	0.597	-0.153	30	0.656	0.646	0.010
11	0.550	0.586	-0.036	31	0.638	0.645	-0.007
12	0.637	0.631	0.006	32	0.668	0.657	0.011
13	0.637	0.632	0.005	33	0.671	0.662	0.009
14	0.653	0.641	0.012	34	0.674	0.667	0.007
15	0.662	0.647	0.015	35	0.687	0.680	0.007
16	0.670	0.658	0.012	36	0.680	0.650	0.030
17	0.681	0.672	0.009	37	0.683	0.673	0.010
18	0.670	0.662	0.008	38	0.297	0.377	-0.080
19	0.623	0.590	0.033	39	0.570	0.620	-0.050
20	0.672	0.663	0.009				

3.5. Testbed D

In testbed D, the buildings in the LiDAR data and fisheye lens photos were removed (Fig. 16). In this testbed, SVF was calculated using 39 fisheye lens photographs and terrestrial LiDAR at the same points (Table 13) without the data of buildings. The SVF error at testbed A has a mean, maximum, and minimum value of 0.062, 0.238, and 0.001, respectively. About 80% showed an error range of less than 0.1. High R2 (0.9275) and a small value of RMSE (0.086) indicate that the SVFt is close to the SVFf.
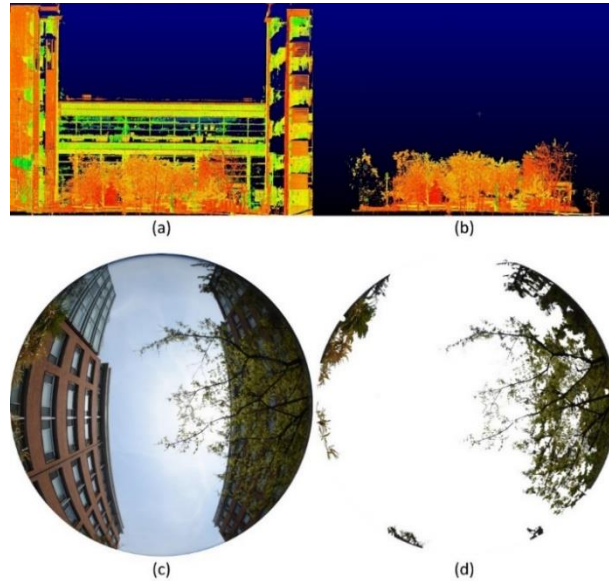
Fig. 16 Before and after building removals: (a) LiDAR data of testbed C, (b) LiDAR data of testbed D, (c) Fisheye lens image of testbed C point 10, (d) Fisheye lens image of testbed D point 10.

Table 13. Computed SVF and difference between SVFt and SVFf in testbed D.

Point (ID)	SVFt (T)	SVFf (F)	SVF Difference (T)-(F)	Point (ID)	SVFt (T)	SVFf (F)	SVF Difference (T)-(F)
1	0.711	0.837	-0.126	21	0.961	0.970	-0.009
2	0.749	0.821	-0.072	22	0.967	0.979	-0.012
3	0.379	0.614	-0.235	23	0.967	0.978	-0.011
4	0.663	0.813	-0.150	24	0.957	0.952	0.005
5	0.742	0.843	-0.101	25	0.961	0.962	-0.001
6	0.852	0.895	-0.043	26	0.961	0.964	-0.003
7	0.758	0.909	-0.151	27	0.953	0.965	-0.011
8	0.881	0.967	-0.086	28	0.958	0.990	-0.032
9	0.875	0.964	-0.089	29	0.958	0.963	-0.005
10	0.615	0.854	-0.239	30	0.925	0.939	-0.014
11	0.751	0.846	-0.095	31	0.863	0.895	-0.032
12	0.847	0.923	-0.075	32	0.916	0.969	-0.053
13	0.857	0.901	-0.044	33	0.917	0.967	-0.049
14	0.885	0.920	-0.035	34	0.913	0.978	-0.065
15	0.904	0.927	-0.022	35	0.946	0.967	-0.022
16	0.936	0.958	-0.022	36	0.912	0.958	-0.046
17	0.952	0.988	-0.035	37	0.925	0.974	-0.049
18	0.954	0.975	-0.021	38	0.449	0.651	-0.202
19	0.937	0.956	-0.019	39	0.669	0.812	-0.142
20	0.962	0.972	-0.009		0.961	0.970	-0.009

Overall, SVF values were increased because buildings were removed. The large increment means that the ratio of buildings blocking the sky is high, and the buildings are located at the center of the fisheye lens photo. In contract, a small increment in SVF relates to the proportion of trees being relatively high.

3.6. Accuracy

SVFt is relatively accurate in testbed A compared with other testbeds. The main difference between testbed A and other testbeds is the inclusion of trees. Trees are the main cause for lack of accuracy. Complicated geometrical shape and leaves in the canopy make trees a key challenging factor in SVF calculation (Kidd and Chapman 2012; An et al. 2014). They also block the sky as obstacles; however, many small gaps between leaves make it difficult to compute SVF accurately.
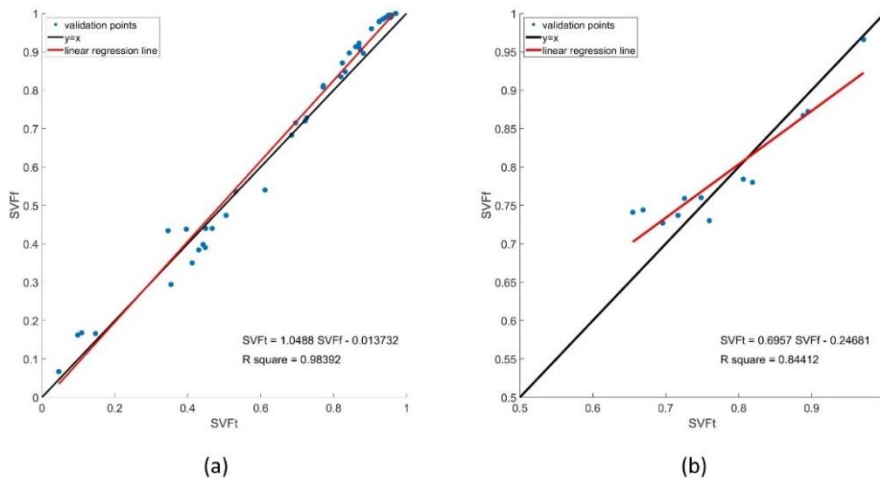
Fig. 17 Scatter plot, linear regression line and ideal line between the SVFt and SVFf: (a) testbed A, (b) testbed B.
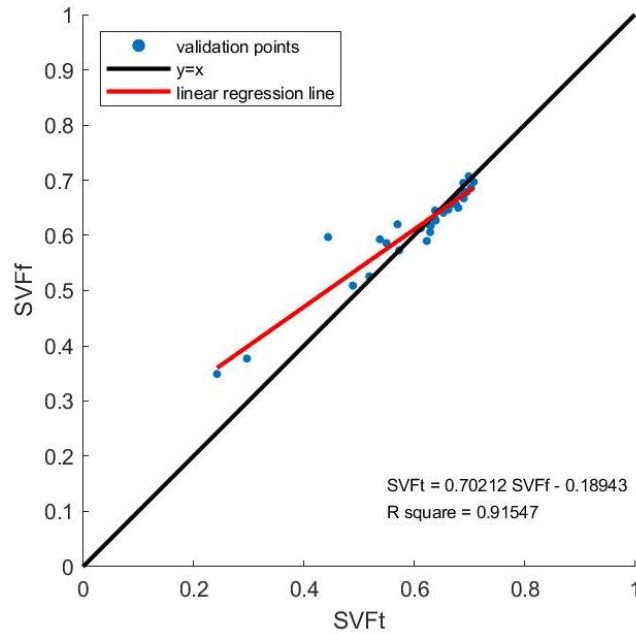
Fig. 18 Scatter plot, linear regression line and ideal line between the SVFt and SVFf at testbed C. Few points were distance away from the ideal line.

In testbeds B and C, graphs show that errors are higher at lower SVF than higher (Fig. 17 and Fig. 18). It is assumed that a lower SVF means more trees near the verification points, which exacerbate the error. Table 12 and Fig. 18 show that most of the verification points fit the ideal line, with the exception of 3 points having a point ID of 3, 10, and 38 (Fig. 19). Trees with many gaps were located at the center of verification points 3, 10 and 38, which lead to the high value of error.
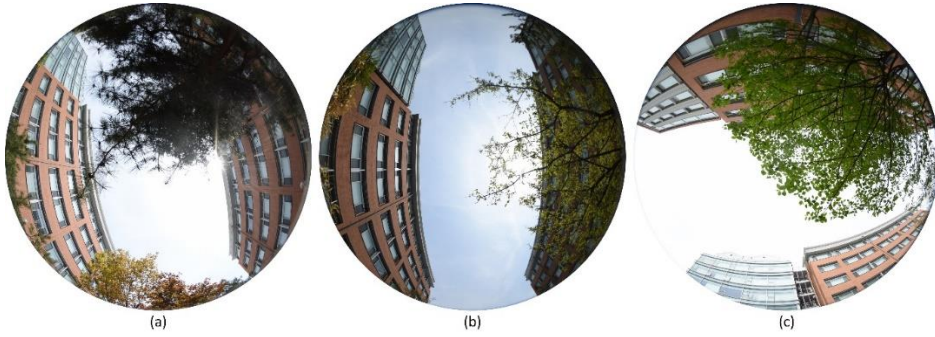
Fig. 19 Fisheye lens images at testbed C: (a) point 3, (b) point 10, (c) point 38.

SVFt = 0.58058 SVFf - 0.42023
R square = 0.92753
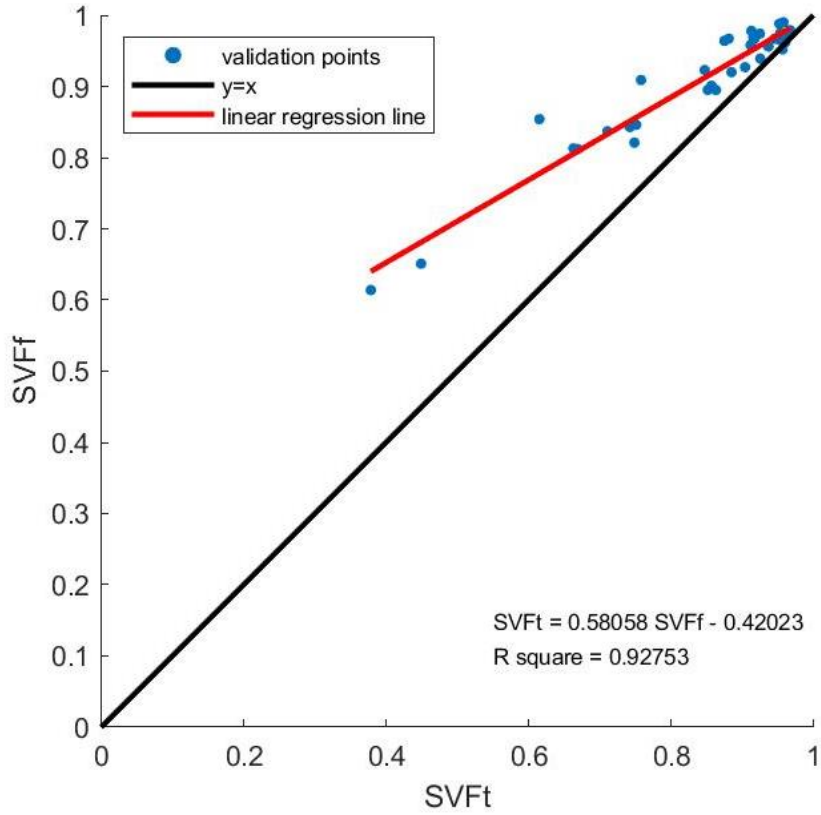
Fig. 20 Scatter plot, linear regression line and ideal line between the SVFt and SVFf at testbed D. Points with lower SVF were more overestimated than the points with higher SVF.

The graph of testbed D shows that errors are higher at lower SVF than higher (Fig. 20). Different from other testbeds, SVFf was higher than SVFt at all points. Moreover, errors were large at point ID 3, 10, and 38 similar to testbed C.

3.7. Sensitivity analysis
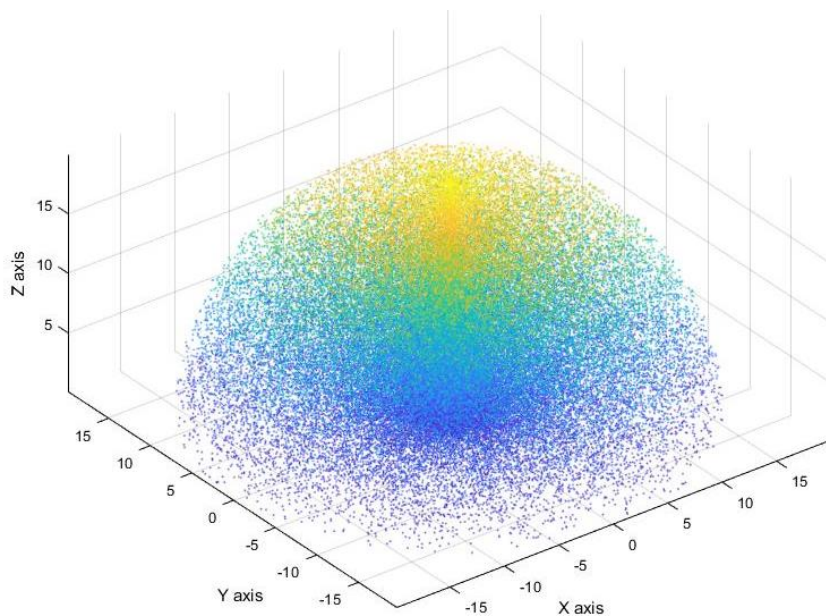
Fig. 21 created 100,000 random points. The points were randomly generated at a distance between 1-20 m from the analysis point (0, 0). The analysis was done by calculating the contribution to the SVF by point.

The SVF reduction effect of each randomly generated 100,000 points (Fig. 21) was computed (Table 14). Larger the voxel size, higher the SVF reduction. In the case of ray interval of 0.5°, which had the highest accuracy, the SVF decreased by 5.25, 20.09, and 74.66 when the voxel size was 5, 10, and 20 cm, respectively. In other words, doubling the voxel size increased the SVF reduction effect by about four times.

Contrary to voxel size, when the ray interval increases, the SVF reduction effect is weakened. With a voxel size of 5 cm and the ray interval doubled, SVF reduction decreases by 80% - 90%. In case of a 10 cm and 20 cm voxel, the SVF reduction decreases by 80% - 95% with the ray interval doubled.

Table 14. Total sum of SVFs lowered by points (100,000 points).

		Ray interval				
		0.5 °	1 °	2 °	4 °	8 °
Voxel size	5cm	5.25	4.67	3.99	3.40	2.84
	10cm	20.09	18.66	16.38	13.65	11.33
	20cm	74.66	70.91	64.65	55.75	45.06

The degree of underestimation/overestimation of 5cm objects is summarized according to the analysis conditions (Table 15). In summary, when the voxel size is increased, the size of the object is overestimated, and when the ray interval is increased, the size of the object is underestimated. For example, a 5 cm object is overestimated by 3.8 times when analyzed at 10cm voxel size.

Table 15. Error rate of each analysis condition based on 0.5 degree 5cm condition.

		Ray interval				
		0.5 °	1 °	2 °	4 °	8 °
Voxel size	5cm	1.0	0.9	0.8	0.6	0.5
	10cm	3.8	3.6	3.1	2.6	2.2
	20cm	14.2	13.5	12.3	10.6	8.6

4. Discussion

Terrestrial LiDAR based SVF estimation has better accuracy than aerial LiDAR and GIS based estimation. The accuracy of SVF estimation using terrestrial LiDAR is not precise, however, it is more accurate than other methods. In high-density urban areas, GIS based SVF estimation, which

calculates SVF with vector data, was highly overestimated, particularly in high-rise areas (Gong et al. 2018). This is because the complexity of urban structures is extremely difficult to capture with a generalized GIS file. Other studies done in a similar environment using aerial LiDAR having both trees and buildings, achieved a maximum error of 0.26 (Kidd and Chapman 2012; An et al. 2014). This study observed a lower error of 0.156 by using the terrestrial LiDAR. Moreover, it is possible to map the estimated SVF continuously, similar to previous GIS methods.

Trees are the main cause of major errors. This research have investigated to determine which of the artificial structures and natural occurrences are the main factors in decreasing accuracy, because they are the main drivers of SVF change in urban areas (Kidd and Chapman 2012). Comparing the results of testbeds C and D, the error increased after removing the data of buildings (Fig. 17 and Fig. 18). Put differently, after this study removed the data of buildings, trees were the only obstacles that blocked the sky, and this area was larger than before increasing the error. Thus this study can conclude that trees are

the main cause of error.

A possible alternative would be to make another testbed without the data of trees. Though it is possible to remove the trees in the terrestrial LiDAR data, removing them from the fisheye lens photography is impossible. To make a testbed with no tree condition, this study must remove the data of trees and restore the data of buildings obscured by trees. In this process, this study could not confirm the presence of buildings in areas of tree removal. Hence, this study could not build an additional testbed.

Testbeds B and D have vegetation as the only condition and have an RMSE of 0.04 and 0.089 respectively, and a higher error in testbed D. The main difference between the two testbeds is that B is indoors and D is outdoors. Outdoor conditions are affected by wind which reduces the data accuracy of terrestrial LiDAR (Dassot et al. 2011) thereby increasing the SVF estimation error. Additionally, trees relative to testbed B are included in testbed D, having smaller leaves and branches. From this perspective, the voxel size and ray interval may not be appropriate to reflect smaller leaves and branches.
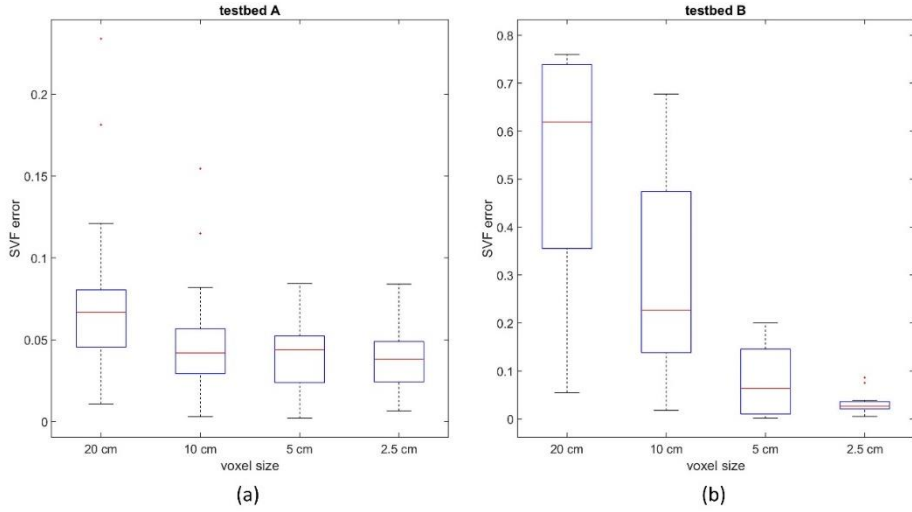
Fig. 22 Boxplot of voxel size effect on absolute error in testbed A and testbed B at a 0.5 degree ray interval.

Voxel size and ray interval are the most important factors that affect SVF accuracy. Therefore, SVF computations were conducted with different voxel sizes and ray intervals using same method as previously applied. At a ray interval of 1°, and reduction in the voxel size, SVF errors decreased (Fig. 22). In testbed A, the error significantly decreased when the voxel size was reduced from 20 cm to 10 cm. The change in error is not substantially observed at the voxel size of 10, 5, and 2.5 cm (Fig. 22a). In testbed B, the error decreased significantly as the voxel size was reduced (Fig. 22b). This is

due to the condition difference between testbed B, with trees, and testbed A,

without trees. Because of the complexity of the tree canopy, testbed B needs

greater resolution than testbed A, to decrease this error. Unlike voxel size, ray

interval does not affect the SVF accuracy in both testbeds A and B, at a fixed

voxel size of 2.5 cm (Fig. 23).
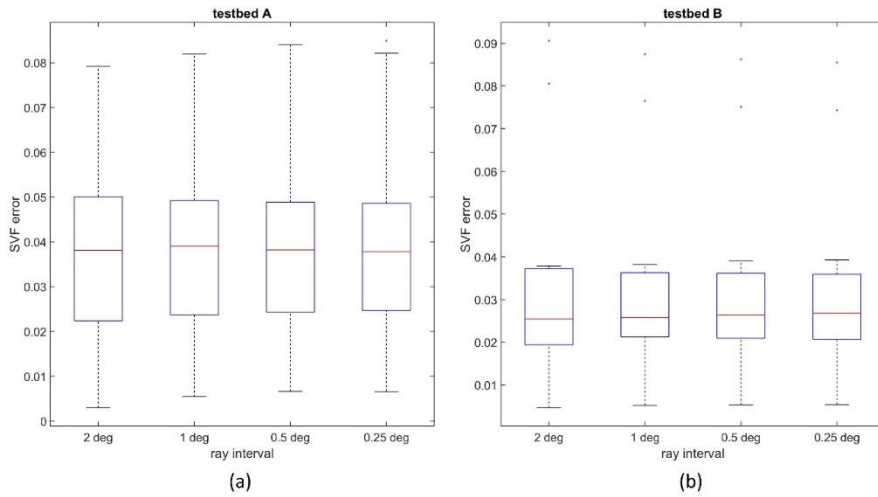
Fig. 23 Boxplot of ray interval effect on absolute error in testbed A and testbed B at 2.5 cm
voxel size.

Based on the resolution effect on SVF accuracy, this research computed 3 verification points at testbed C, which had high errors. Points 3, 10 and 38 were computed at a fixed voxel size of 2.5 cm with 1° of ray interval. The SVF errors decreased (Fig. 24) to 0.011, 0.039, and 0.069 at points 3, 10, and 18, respectively. Unlike others, the degree of improvement in the result was small at point 3. It is considered that the effect of needle leaf tree at point 3 makes the error higher as its leaf is thin and long, its covered area would be overestimated, and thus needs a smaller voxel size to reduce the error.
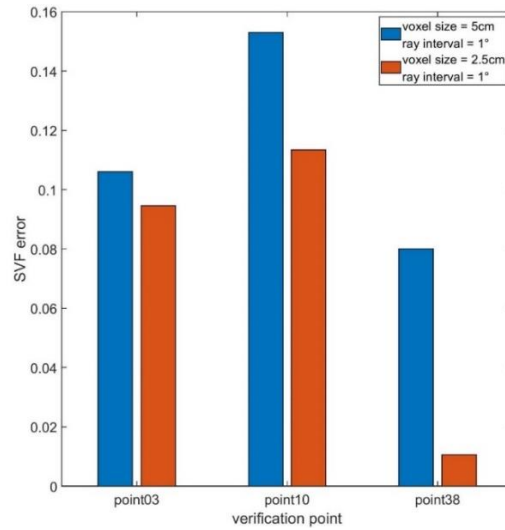
Fig. 24 SVF errors at different voxel size in testbed C at point 3, point 10, and point 38. Reducing the voxel size reduced the error at all points.

It seems that resolution of the LiDAR data and voxel size are important to improve accuracy. However, with high-resolution data, the size of data becomes larger, thus requiring a longer time for analysis. Therefore, using unconditional high-resolution data would not be the best choice. The results dictate that high-resolution data is required only when there are trees having a large canopy area. Therefore, we need to calculate SVF with appropriate resolution to reflect local characteristics.

In sensitivity analysis, the voxel size and ray interval were selected as variation variables. Voxel size indicates how accurately the real object can be reflected in the analysis. As the voxel size increases, the small object in reality is overestimated. According to sensitivity analysis, an object that is 5 cm in reality is overestimated by four times when analyzed at a voxel size of 10 cm (Table 14). However, this corresponds to one point in real data, and points will have adjacent points that result in lower overestimation by four times. That is, thin and small objects such as branches or leaf can cause overestimation by up to four times. As a result, overestimation of object size

will result in underestimation of SVF.

The ray interval determines how accurately the voxel can be detected. The smaller the ray interval, the more it can detect farther and smaller objects. As the ray interval gets larger, the probability of not detecting increases, which causes an underestimated object size and overestimated SVF.

This research also needs to consider the application of Mobile LiDAR. With this paper, this study have established that high accuracy is obtained at a voxel size of 2.5 cm. Mobile LiDAR system, wherein LiDAR is mounted on moving vehicles, can scan large urban areas at a resolution equal to terrestrial LiDAR (Zhao et al. 2018). Therefore, SVF estimation using mobile LiDAR is expected to have similar accuracy as terrestrial LiDAR. However, since terrestrial LiDAR and mobile LiDAR have different data acquisition methods, additional research is required.

V. Developing a method to construct urban scale data with high accuracy using LiDAR: SVF and GVI on the street

1. Scope of study

Point cloud enable to construct data in the form of a continuous map with high resolution. However, constructing data on an urban scale requires high volumes of data and analysis time. Urban scale data at high resolution is important, but for better efficiency, it may be better to analyze faster, even at lower resolutions. This research tried to identify the better way to construct the data for urban scale even if the resolution is slightly lowered. In addition, this research tried to analyze how to maintain the accuracy of the values even when the resolution is lowered.

A simulation framework in a controlled virtual environment was employed to achieve the objectives of this study because it was not otherwise possible

to assume the uniform conditions necessary for this type of research. This approach was due to the uneven arrangement of trees and buildings, which would cause potential measurement errors in analyzing SVF and GVI. Conversely, a controlled virtual site would be flexible to simulate various physical conditions, unlike an actual site. It was also able to exclude the influence of other factors affecting the SVF and GVI values.

A virtual site of this study was constructed by using a voxelized 3D point cloud. The 3D point cloud represented objects in the form of points. The data complied through light detection and ranging (LiDAR) were stored in this data type. This approach offered us the advantage that actual objects scanned by LiDAR could be used at the virtual site. In this study, virtual cylindrical trees and real trees scanned by terrestrial LiDAR were both applied in the simulation. Gingko (*Gingko biloba*) was used for scanned tree and CBH estimation algorithm was applied to classify crown part of the tree.

Various site settings and measurement points were considered to investigate the variations in the SVF and GVI estimation. The SVF is affected

by the distance from surrounding trees and buildings, as well as the spacing between trees. The GVI is affected by the distance from surrounding trees and the spacing between trees. Therefore, to examine the influence of the distance from the surrounding trees and buildings, this research designed research areas considering various road widths, tree spacing for GVI estimation simulation. For SVF estimation simulation, various building heights were additionally considered. In addition, the SVF and GVI could differ because the distances from the surrounding trees depending on the location of the measurement point, even within the same research area. In order to reflect this issue, this research monitored changes in the SVF and GVI according to the measurement point by considering various measurement points within each research setting.

In the GVI analysis, setting the buffer distance is crucial in terms of calculation accuracy and time. This study first derived the appropriate buffer distance. In order to determine the buffer distance, this study conducted a sensitivity analysis to estimate the GVI by applying different buffer distances

ranging from 30 m to 302 m at intervals of 16 m for road widths of 7.5 m, 15 m, 22.5 m, and 30 m. As a result, 150 m was selected as an appropriate buffer for the GVI analysis.

2. Research area setting

This research created a total of 40 research settings (Fig. 25). This research considered road width, tree planting interval, and tree type. The road width was set to range between 2 and 8 lanes with a 2-lane interval. The widths of the sidewalk and road were set at 5 m and 3.75 m, respectively (Fitzpatrick et al. 2001). It was assumed that the sidewalks were located on both sides of the road and street trees were planted out at equal intervals along the sidewalks within 1 meter from the edge of the road.

Road width (4 conditions)		Tree interval (5 conditions)		Tree type (2 conditions)		Total
7.5m		4m		Virtual tree		Total
15m	X	6m	X		=	40 research areas
22.5m		8m				
		10m				
30m		12m		Real tree		
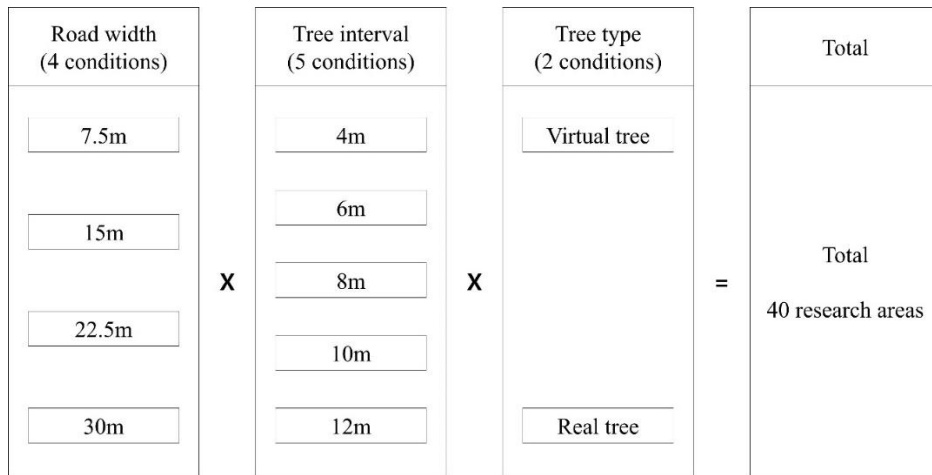
Fig. 25 Schematic diagram of the site conditions for 40 research site settings.

In urban areas, different types of trees can be planted at various intervals. To reflect this situation, various planting patterns were set for each research site. At first, because the SVF and GVI would change based on the distance between the trees, those distances were set to range between 4 m to 12 m at 2 m increments.

Additionally, this research analyzed different cases of virtual trees with cylindrical canopy and cases with LiDAR-scanned trees. As a result, 40 different research settings were developed for this research by applying five different tree-planting intervals and two tree types to each of the four sites. In

addition to 40 research areas, the SVF study additionally applied 10m, 20m, and 30m height buildings to the simulation. As a result, a total of 120 research areas were created in the SVF study.

3.   Method

3.1. SVF estimation

The SVF was estimated using the algorithm described in chapter IV.2.2. Different from previous chapter, research area of this chapter is voxelized 3D point cloud data which have 20cm voxel size.

3.2. GVI estimation

The GVI was estimated by creating an occlusion map using point cloud data; data points were classified as building, road, sidewalk, or tree (Susaki and Kubota 2017). To generate the occlusion map, the azimuth and elevation angles from the viewpoint were varied from 0° to 360° or −90° to + 90°,

respectively, in 1° increments. Under these conditions, this research computed a visual observation from each angle (Fig. 26). An occlusion map with an azimuth angle as the x-axis and elevation angle as the y-axis was then derived from the objects observed from all angles (Fig. 27). In this occlusion map, the GVI was calculated using the ratio of green pixels to all the pixels. However, this method could cause a high number of errors near the elevation angles of −90° and +90° (Susaki and Kubota 2017). Therefore, this research applied an equisolid angle projection to reduce such errors (Susaki et al. 2014; Susaki and Kubota 2017).
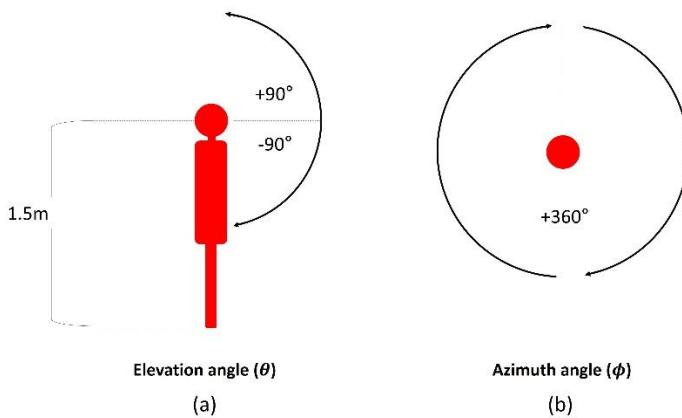
Fig. 26 Measurement range at the GVI measurement point.
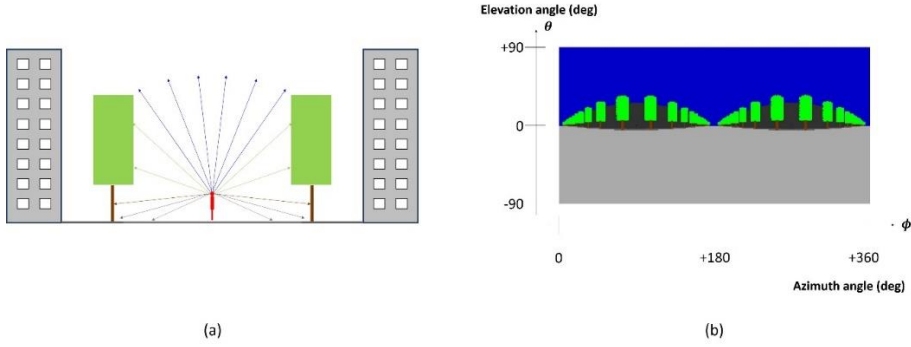
Fig. 27 Occlusion map for estimating the GVI.

Unlike the existing method of dividing a space by the same angular interval in the azimuth-elevation angle space, the equisolid angle projection generates the unit areas in the space equal. This research converted the azimuth-elevation angle space data to the equisolid-angle projected space (Fig. 27) and applied Equation 1 to compute the GVI.

$$\text{GVI} = \frac{\sum_{\emptyset=0}^{360-\Delta\emptyset} \sum_{\theta=-90}^{90} ds(\emptyset,\theta) f(\emptyset,\theta)}{\sum_{\emptyset=0}^{360-\Delta\emptyset} \sum_{\theta=-90}^{90} ds(\emptyset,\theta)} \times 100, \tag{1}$$

where $\emptyset$ and θ denote the azimuth and elevation angles, respectively, in the azimuth-elevation angle space, respectively, and $ds(\emptyset,\theta)$ denotes the area of a cell in the equisolid-angle projected space. It is given by:

$$ds(\emptyset, \theta) = (Rcos\theta\Delta\emptyset) = R^2cos\theta\Delta\emptyset\Delta\theta, \qquad\qquad (2)$$

where R denotes the radius of a sphere upon which the projected elements

are assumed to be located on, and $f(\emptyset, \theta)$ denotes a function of the occlusion

given by:

$$f(\emptyset, \theta) = \begin{cases} 1 : & occluded \\ 0 : & not\ occluded \end{cases}, \qquad\qquad (3)$$

According to Equation 1, the GVI can vary from 0% to 100%.

3.3. Observation points
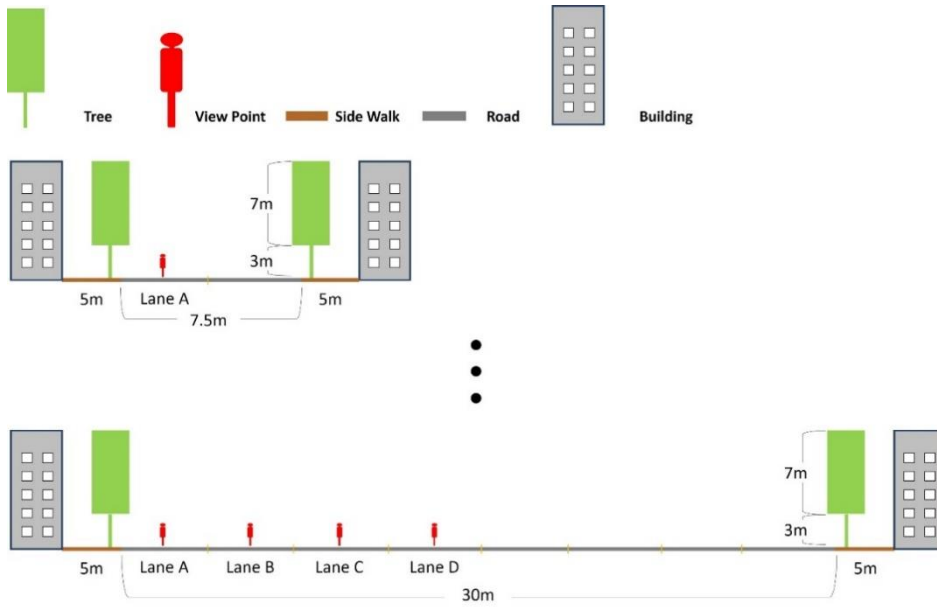
Fig. 28 Basic conditions of the research area and horizontal GVI measurement positions.

This research measured the SVF and GVI values on the road. The values were different depending on the horizontal (Fig. 28) and vertical (Fig. 29) measurement positions. Measurement points can be obtained from various positions on a road, and the SVF and GVI differed depending on the point at which the photograph was taken. The study area setting was symmetrical around the center line, the SVF and GVI were analyzed in the middle of the

lanes from the first to the fourth lane (Fig. 28). In this research, the lanes are referred to as Lane A, Lane B, Lane C, and Lane D, beginning with the side nearest to the sidewalk. This research also considered differences in the vertical position. The vertical position causes a difference in the distance from the line of trees, resulting in a SVF and GVI variation. Therefore, the analysis was carried out for three points: the center of the width of the tree, the point at 3/4th the width of the tree, and the point adjacent to the far end of the tree (hereafter referred to as V1, V2, and V3, respectively) (Fig. 29). Finally, SVF and GVI were analyzed at six points on the 7.5 m-wide road, nine points on the 15 m-wide road, 12 points on the 22.5 m-wide road, and 15 points on the 30 m-wide road.
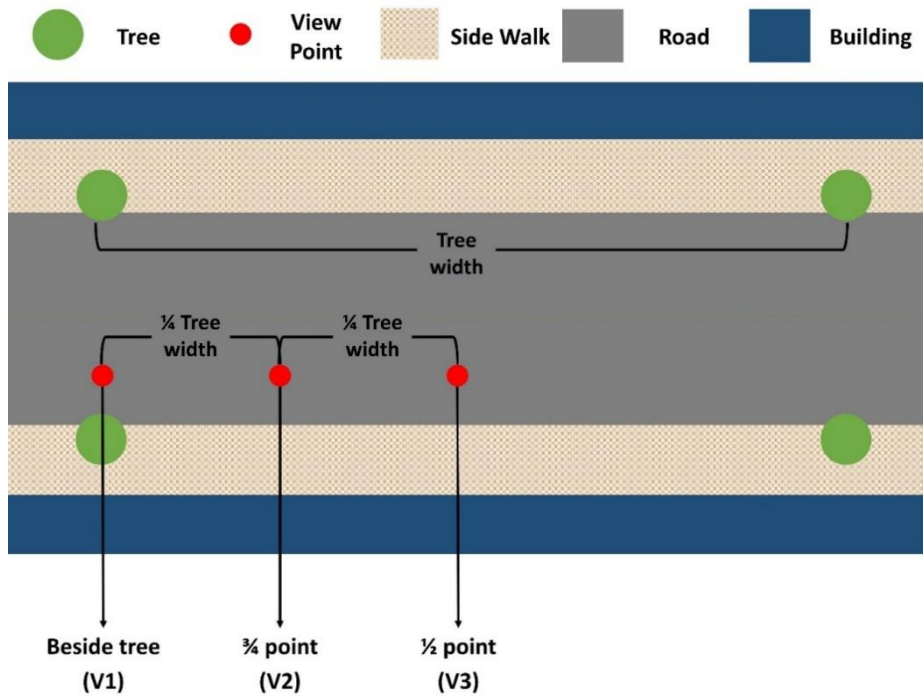
Fig. 29 Vertical GVI measurement positions.

3.4. Statistical analysis

The SVF was estimated from 600 and the GVI was estimated from 300 measurement points on the road. At first, this study calculated the average GVI for each research site to identify the main causes of GVI changes. In addition, to analyze effect of the measurement points of each site on the GVI error range, this study computed the difference between the maximum and

minimum GVI values for each research site. Secondly, this study analyzed

the error range caused by the horizontal and the vertical positions. The

average of the analysis points at the same vertical and horizontal positions in

each research area with a road width of 30m were computed. Finally, in order

to derive the position from which the most representative GVI could be

measured in each research area, this research determined the positions with

values closest to the average GVI values of each research area.

4. Result

4.1. SVF

4.1.1. SVF values as measured from various positions

Both road widths and tree planting intervals were significantly related to

average SVF changes. The average SVF values for 120 research settings were

calculated (Table 22). In general, the SVF was higher when using virtual trees.

The narrower the road and the lower the tree interval, the lower the average

SVF were reported.

Table 16. Average SVF by study setting. As the road width and tree interval increases, the average SVF increases.

Planting condition	Interval (m)	Road width			
		7.5m	15m	22.5m	30m
	4	0.479	0.627	0.707	0.759
	6	0.515	0.648	0.722	0.770
Virtual tree	8	0.538	0.661	0.731	0.777
	10	0.553	0.670	0.737	0.782
	12	0.564	0.676	0.742	0.785
	4	0.320	0.550	0.657	0.721
	6	0.388	0.586	0.682	0.740
Real tree	8	0.434	0.611	0.698	0.752
	10	0.477	0.633	0.713	0.764
	12	0.498	0.644	0.721	0.769

The differences between the maximum and minimum SVF values for each research setting are summarized in Table 23. The wider the road, the greater the difference in SVF value for each site. On the 7.5 m-wide road, the most significant difference occurred when real trees were planted at 12 m intervals; the maximum and minimum GVI values were 0.727 and 0.281, respectively. On the 30 m-wide road, the biggest difference occurred when real trees were planted at 4 m intervals; the maximum and minimum SVF values were 0.940 and 0.408, respectively. Compared to the difference between 7.5m road and 15m road, the difference between 22.5m road and 30m road was smaller.

Table 17. Difference between the maximum and minimum GVI values by study setting.

Planting condition	Interval (m)	Road width			
		7.5m	15m	22.5m	30m
Virtual tree	4	0.099	0.257	0.311	0.331
	6	0.163	0.278	0.316	0.329
	8	0.208	0.293	0.321	0.329
	10	0.241	0.305	0.325	0.330
	12	0.266	0.313	0.327	0.330
Real tree	4	0.147	0.484	0.525	0.532
	6	0.300	0.482	0.512	0.515
	8	0.371	0.485	0.506	0.507
	10	0.416	0.490	0.504	0.504
	12	0.446	0.494	0.504	0.503

4.1.2. Effects of horizontal and vertical road positions on SVF values

A horizontal measurement position on the road caused a SVF difference of up to 0.389 (Table 24). The SVF was highest on Lane D and lowest on Lane A. In other words, the SVF was higher at the points further from the sidewalk and lower when closer to the sidewalk. In particular, the lower the average SVF and the narrower the tree interval, the greater the difference is SVF values. In some cases where real trees were analyzed, the SVF of Lane D was almost twice as high as that of Lane A. That is, the horizontal position

highly affected the SVF difference, and that difference grew larger as the tree interval narrowed.

Table 18. Average SVF values by horizontal position difference in maximum and minimum SVF values.

Planting condition	Interval (m)	Horizontal position				
		Lane A	Lane B	Lane C	Lane D	Max-Min
Virtual tree	4	0.623	0.768	0.813	0.831	0.209
	6	0.652	0.776	0.817	0.834	0.182
	8	0.671	0.781	0.820	0.836	0.165
	10	0.683	0.785	0.821	0.837	0.154
	12	0.692	0.787	0.823	0.838	0.146
Real tree	4	0.450	0.777	0.821	0.838	0.389
	6	0.515	0.782	0.823	0.839	0.324
	8	0.560	0.785	0.824	0.840	0.280
	10	0.602	0.788	0.825	0.841	0.239
	12	0.622	0.789	0.826	0.841	0.219

A vertical measurement position on the road caused a SVF difference of up to 0.063 (Table 25). The SVF was highest in V3 and lowest in V1. Contrary to the horizontal position, the SVF difference was greater when the average SVF was higher and tree interval was wider. The SVF difference caused by the vertical position was much smaller than that caused by the horizontal position.

Table 19. Average SVF values by vertical position and differences in maximum and minimum SVF values.

Planting condition	Interval (m)	Vertical position			
		V1	V2	V3	Max-Min
	4	0.823	0.824	0.826	0.003
	6	0.844	0.848	0.851	0.006
Virtual tree	8	0.859	0.863	0.867	0.009
	10	0.867	0.874	0.879	0.012
	12	0.872	0.882	0.887	0.015
	4	0.796	0.799	0.800	0.004
	6	0.810	0.813	0.848	0.038
Real tree	8	0.821	0.838	0.870	0.049
	10	0.827	0.866	0.885	0.058
	12	0.831	0.880	0.894	0.063

Unlike the horizontal position, the distance between vertical positions differed depending on the research settings. Concerning the horizontal position, the distance between the analysis points of Lanes A, B, C, and D was 3.75 m, which was equal to the road width. On the other hand, concerning the vertical position, the distance between the analysis points for V1, V2, and V3 varied from 1 m to 3 m. In other words, the wider the planting interval, the greater the distance between the analysis points and difference in SVF values. Nevertheless, the maximum vertical position influence of 0.063 indicates that the vertical position effect was minimal compared to that of the horizontal position.

4.1.3. What position best represents the research setting?

In order to identify the representative estimation points, the SVF values closest to the average SVF for each research setting were selected (Table 26). The horizontal position was found to be a major factor in determining the most representative estimation point. In research areas with a 15 m road width where two horizontal positions existed, all representative estimation points were located in Lane A. In the research areas with the 22.5 m, 7 out of 10 representative estimation points were located in Lane B. 30 m road widths, all representative estimation points were located in Lane B. Conversely, it was difficult to find a specific trend in analyzing vertical positions, except in rare cases. This is because the horizontal position had a greater influence on the GVI value than did the vertical position.

Table 20. Estimation points closest to the average SVF values. The horizontal and vertical positions can be used to specify points within the study site.

Planting condition	Interval (m)	Road width			
		7.5m	15m	22.5m	30m
Virtual tree	4	Lane A V2	Lane A V3	Lane B V3	Lane B V3
	6	Lane A V2	Lane A V3	Lane B V3	Lane B V3
	8	Lane A V2	Lane A V3	Lane B V1	Lane B V3
	10	Lane A V2	Lane A V3	Lane B V1	Lane B V1
	12	Lane A V2	Lane A V3	Lane B V1	Lane B V1
Real tree	4	Lane A V2	Lane A V3	Lane B V3	Lane B V3
	6	Lane A V2	Lane A V3	Lane B V2	Lane B V2
	8	Lane A V2	Lane A V3	Lane A V3	Lane B V1
	10	Lane A V2	Lane A V3	Lane A V3	Lane B V1
	12	Lane A V2	Lane A V3	Lane A V3	Lane B V1

Based on Table 26, representative estimation points for each road width were set. The maximum differences between the average SVF and SVF for Lane A on 15m, Lane B on 22.5 m and 30 m roads were used as representative SVF values. As a result, the maximum and average differences were 0.172 and 0.034 respectively (Table 27).

Table 21. Maximum difference in SVF from a representative estimation point and average SVF by study setting.

Planting condition	Interval (m)	Building height 10m			Building height 20m			Building height 30m		
		Road width(m)								
		15	22.5	30	15	22.5	30	15	22.5	30
Virtual tree	4	0.069	0.039	0.005	0.068	0.043	0.018	0.036	0.023	0.005
	6	0.052	0.034	0.006	0.053	0.035	0.012	0.027	0.018	0.001
	8	0.040	0.030	0.005	0.043	0.029	0.008	0.023	0.016	0.000
	10	0.030	0.027	0.004	0.035	0.026	0.006	0.020	0.015	0.001
	12	0.021	0.023	0.003	0.029	0.023	0.004	0.018	0.013	0.002
Real tree	4	0.172	0.104	0.055	0.151	0.101	0.062	0.120	0.080	0.048
	6	0.054	0.087	0.046	0.031	0.079	0.045	0.015	0.062	0.034
	8	0.016	0.081	0.036	0.005	0.058	0.035	0.006	0.037	0.027
	10	0.002	0.056	0.026	0.001	0.048	0.026	0.007	0.031	0.018
	12	0.011	0.039	0.021	0.003	0.041	0.021	0.008	0.027	0.015

4.2. GVI

4.2.1. GVI values as measured from various positions

Both road widths and tree planting intervals were significantly related to average GVI changes. The average GVI values for 40 research settings were calculated (Table 22). In general, the GVI was higher when using real trees. The narrower the road and the lower the tree interval, the higher the average GVI were reported. Irrespective of the tree interval, the GVI of the narrowest road was nearly twice as high as that of the GVI of the 30 m-wide road width.

Table 22. Average GVI by study setting. As the road width and the tree interval decreases, the average GVI increases.

Planting condition	Interval (m)	Road width			
		7.5m	15m	22.5m	30m
	4	27.4%	22.0%	18.3%	15.7%
	6	21.8%	17.4%	14.3%	12.2%
Virtual tree	8	17.8%	14.1%	11.5%	9.8%
	10	15.0%	11.7%	9.6%	8.1%
	12	12.9%	10.1%	8.2%	6.9%
	4	31.1%	23.6%	19.1%	16.1%
	6	27.8%	20.9%	16.8%	14.1%
Real tree	8	23.4%	17.4%	13.9%	11.7%
	10	19.6%	14.6%	11.6%	9.7%
	12	16.7%	12.4%	9.9%	8.3%

The differences between the maximum and minimum GVI values for each research setting are summarized in Table 23. The wider the road, the greater the difference in GVI value for each site. On the 7.5 m-wide road, the most significant difference occurred when real trees were planted at 12 m intervals; the maximum and minimum GVI values were 19.3% and 14.4%, respectively. On the 30 m-wide road, the biggest difference occurred when real trees were planted at 4 m intervals; the maximum and minimum GVI values were 23.3% and 11.7%, respectively. In addition, as the road widened, the difference between the maximum and minimum GVI values for each research setting tended to increase.

Table 23. Difference between the maximum and minimum GVI values by study setting.

Planting condition	Interval (m)	Road width			
		7.5m	15m	22.5m	30m
Virtual tree	4	0.4%p	1.1%p	3.8%p	6.0%p
	6	1.1%p	1.7%p	3.7%p	5.6%p
	8	1.3%p	1.9%p	3.6%p	5.1%p
	10	1.8%p	2.1%p	3.6%p	4.8%p
	12	2.5%p	2.5%p	3.6%p	4.7%p
Real tree	4	0.3%p	6.2%p	9.6%p	11.6%p
	6	0.7%p	5.9%p	9.1%p	11.1%p
	8	1.8%p	5.5%p	8.1%p	9.9%p
	10	3.2%p	5.4%p	7.6%p	9.0%p
	12	4.9%p	5.7%p	7.5%p	8.7%p

4.2.2. Effects of horizontal and vertical road positions on GVI values

A horizontal measurement position on the road caused a GVI difference of up to 11.6%p (Table 24). The GVI was highest on Lane A and lowest on Lane D. In other words, the GVI was higher at the points closer to the sidewalk and lower when further from the sidewalk. In particular, the higher the average GVI and the narrower the tree interval, the greater the difference is GVI values. In some cases where real trees were analyzed, the GVI of Lane A was more than twice as high as that of Lane D. In addition, the GVI of Lane A was sometimes 1.5 times higher than that of Lane D when virtual trees were tested. That is, the horizontal position highly affected the GVI difference, and that difference grew larger as the tree interval narrowed.

Table 24. Average GVI values by horizontal position difference in maximum and minimum GVI values.

Planting condition	Interval (m)	Horizontal position				
		Lane A	Lane B	Lane C	Lane D	max-min
Virtual tree	4	18.7%	16.4%	14.3%	13.1%	5.6%p
	6	15.0%	12.8%	11.0%	10.1%	4.9%p
	8	12.4%	10.2%	8.6%	7.9%	4.4%p
	10	10.4%	8.4%	7.2%	6.5%	3.9%p
	12	8.9%	7.2%	6.0%	5.5%	3.4%p
Real tree	4	23.4%	16.1%	13.1%	11.8%	11.6%p
	6	20.8%	14.2%	11.3%	10.2%	10.7%p
	8	17.3%	11.7%	9.3%	8.3%	9.0%p
	10	14.4%	9.8%	7.7%	6.9%	7.5%p
	12	12.3%	8.3%	6.6%	5.9%	6.4%p

A vertical measurement position on the road caused a GVI difference of up to 1.2% (Table 25). The GVI was highest in V1 and lowest in V3. Contrary to the horizontal position, the GVI difference was greater when the average GVI was lower and tree interval was wider. The GVI difference caused by the vertical position was much smaller than that caused by the horizontal position.

Table 25. Average GVI values by vertical position and differences in maximum and minimum GVI values.

Planting condition	Interval (m)	Vertical position			
		V1	V2	V3	Max-Min
Virtual tree	4	15.7%	15.6%	15.6%	0.1%p
	6	12.4%	12.2%	12.1%	0.4%p
	8	10.0%	9.7%	9.6%	0.3%p
	10	8.3%	8.1%	7.9%	0.4%p
	12	7.3%	6.9%	6.6%	0.7%p
Real tree	4	16.1%	16.2%	16.2%	0.1%p
	6	14.3%	14.1%	14.1%	0.2%p
	8	11.9%	11.7%	11.4%	0.4%p
	10	10.1%	9.7%	9.4%	0.8%p
	12	8.9%	8.2%	7.7%	1.2%p

4.2.3. What position best represents the research setting?

In order to identify the representative estimation points, the GVI values closest to the average GVI for each research setting were selected (Table 26). The horizontal position was found to be a major factor in determining the most representative estimation point. In research areas with a 15 m road width where two horizontal positions existed, 9 out of 10 representative estimation points were located in Lane A. In the research areas with the 22.5 m and 30 m road widths, all representative estimation points were located in Lane B. It was difficult to find a specific trend in analyzing vertical positions, except in

rare cases. This is because the horizontal position had a greater influence on

the GVI value than did the vertical position.

Table 26. Estimation points closest to the average GVI values.

Planting condition	Interval (m)	Road width			
		7.5m	15m	22.5m	30m
Virtual tree	4	Lane A V2	Lane A V3	Lane B V3	Lane B V1
	6	Lane A V2	Lane A V3	Lane B V1	Lane B V2
	8	Lane A V2	Lane A V3	Lane B V1	Lane B V3
	10	Lane A V2	Lane A V3	Lane B V2	Lane B V2
	12	Lane A V2	Lane B V1	Lane B V1	Lane B V3
Real tree	4	Lane A V3	Lane A V1	Lane B V3	Lane B V1
	6	Lane A V2	Lane A V3	Lane B V1	Lane B V3
	8	Lane A V2	Lane A V3	Lane B V1	Lane B V2
	10	Lane A V2	Lane A V3	Lane B V1	Lane B V3
	12	Lane A V2	Lane A V3	Lane B V1	Lane B V2

Based on Table 26, representative estimation points for each road width

were set. The maximum differences between the average GVI and GVI for

Lane A on 15m, Lane B on 22.5 m and 30 m roads were used as representative

GVI values. As a result, the differences in the average GVI for the research

setting decreased to 3% (Table 27).

Table 27. Maximum difference in GVI from a representative estimation point and average GVI by study setting

Planting condition	Interval (m)	Road width		
		15m	22.5m	30m
	4	0.4%p	0.1%p	0.8%p
	6	0.5%p	0.2%p	0.6%p
Virtual tree	8	0.6%p	0.2%p	0.4%p
	10	0.6%p	0.3%p	0.3%p
	12	0.5%p	0.2%p	0.2%p
	4	3.0%p	1.5%p	0.0%p
	6	2.7%p	1.3%p	0.1%p
Real tree	8	2.3%p	1.1%p	0.0%p
	10	1.9%p	0.9%p	0.1%p
	12	1.6%p	0.8%p	0.0%p

5. Discussion

According to the analysis of SVF and GVI in the urban street, values are

different depending on the position even within the small target area on the

road. Lowering the resolution of such data and extending it to the urban scale

can lead to high uncertainty. Based on the results of this study, urban scale

data construction can be accomplished in two ways. Firstly, researcher can choose where the researcher want to get results. For example, if a researcher want data from the center of the street, researcher can get the data by analyzing it in the center of the street at regular intervals. Secondly, representative points can be used as derived from this study.

One of the things that makes urban scale analysis possible is that the vertical position has little effect on the variation. Accordingly, if the horizontal position is selected in the research design, data can be constructed with high accuracy at the urban scale by analyzing at regular vertical intervals. From this point of view, Google Street View (GSV) imagery, which is widely used for urban scale analysis, has its limitations.

In SVF and GVI studies, the lanes from which GSV is taken impact the overall accuracy. Many researchers have used GSV to calculate local SVF and GVI values. However, little information have been documented with regards to road widths and the lanes from which images were taken. The accuracy can be increased by narrowing the collection interval for GSV

images. Since this would control the vertical position rather than horizontal position, however, we expect that the effect on increasing the accuracy would be minimal. Accuracy could be further improved, if the image in the representative lane or position is selected based on the width of the road. However, GSV does not yet provide information such as road width and lane numbers for its images. Nevertheless, there is still some level of accuracy when the road is narrow.

GSV is not only used in SVF and GVI studies but also used in walkability analysis by classifying sky area (Yin and Wang 2016; Wang et al. 2019), neighborhood environment measurement (Odgers et al. 2012) and pedestrian volume measurement (Yin et al. 2015). These studies have something in common in using GSV images, but they differ in the way they are used. Studies using the area occupied by objects classified in the image are considered to be influenced by the lane where the GSV image is taken as shown in this study. On the other hand, the lanes should not be considered in neighborhood environment and pedestrian volume research because they

count objects in the images such as, number of pedestrians or number of speed limit signs.

The lack of consideration of all road conditions is a limitation of this study. In this study, multiple road widths, tree intervals, and building heights were considered on straight roads. However, there are other roads in the city other than straight roads such as curved roads and intersections. Curved roads and intersections may have different characteristics than straight roads covered in this study. Concerning different conditions, further analysis needs to be done to investigate the method for urban scale data construction. Nevertheless, because the straight road is the most common road type in the urban area, this study has contribution to urban scale data construction study.

VI. Conclusion

This study explores the possibility of measuring SVF and GVI in urban scale. In addition, as a LiDAR data preprocessing step for GVI analysis, CBH, DBH, tree height were calculated and accuracy assessment was conducted. This study shows the feasibility of constructing accurate data for trees in a wide area using mobile LiDAR. Mobile LiDAR has medium resolution, measurement range and accuracy between airborne LiDAR and terrestrial LiDAR. These characteristics of mobile LiDAR allow researchers to obtain DBH measurement, which is impossible with airborne LiDAR, and qualify more accurate CBH and tree height measurement. Moreover, it is possible to build data at a wider range, which is difficult with terrestrial LiDAR.

For the LiDAR based SVF accuracy evaluation, this research employed terrestrial LiDAR unlike the other studies that employed aerial LiDAR. The accuracy was higher because the terrestrial LiDAR has a higher resolution than that of aerial LiDAR. There are disadvantages as well as advantages to

improving accuracy. It is difficult to scan large area with terrestrial LiDAR because it collects data at a fixed position. According to the result, it is considered that the mobile LiDAR which is convenient for scanning large areas has high enough resolution to estimate SVF accurately. Therefore, SVF calculation technique used in this study will have higher practicality when it comes to mobile LiDAR.

Through identifying the most accurate SVF and GVI average value in a wide area, this study has confirmed the possibility of constructing a city-level inventory. To scale up the method that this study offered, accurate data can be built over a large area while minimizing the amount of computation load. On the other hand, data quality such as point density and accuracy will be an important issue as investigated in sensitivity analysis.

The computation time can be the main issue in a large scale data construction. Computation time is highly dependent on data size, computing power, required resolution (ray interval, SVF and GVI map resolution, point cloud data resolution). This research investigated the resolution effect on the

SVF and GVI, and studied ways to reduce the error of the results. However, the optimum resolution was not obtained. In order to find the optimal resolution, a reasonable error range is required. In other words, further research is needed to determine the required accuracy of SVF and GVI calculations.

The urban environment has various variables in addition to those discussed in this study and SVF and GVI can be affected by them. For example, seasonal changes in vegetation have a significant impact on the SVF and GVI. Also, during summer, one tree may obscure another, making it difficult to collect LiDAR data itself, and the final result may be affected by it. Nevertheless, it is impossible to consider all the conditions of the urban street environment. It is necessary to solve important factors in order, and this study will be the starting point.

VII. Bibliography

An SM, Kim BS, Lee HY, et al (2014) Three-dimensional point cloud based sky view factor analysis in complex urban settings. Int J Climatol 34:2685–2701. https://doi.org/10.1002/joc.3868

Anaya JA, Chuvieco E, Palacios-Orueta A (2009) Aboveground biomass assessment in Colombia: A remote sensing approach. For Ecol Manage 257:1237–1246. https://doi.org/10.1016/j.foreco.2008.11.016

Bernard J, Bocher E, Petit G, Palominos S (2018) Sky View Factor Calculation in Urban Context: Computational Performance and Accuracy Analysis of Two Open and Free GIS Tools. Climate 6:60. https://doi.org/10.3390/cli6030060

Bonnaffe F, Jennette D, Andrews J (2007) A method for acquiring and processing ground-based lidar data in difficult-to-access outcrops for use in three-dimensional, virtual-reality models. Geosphere 3:501–510. https://doi.org/10.1130/GES00104.1

Browning M, Lee K (2017) Within what distance does "greenness" best predict physical health? A systematic review of articles with gis buffer analyses across the lifespan. Int J Environ Res Public Health 14:1–21. https://doi.org/10.3390/ijerph14070675

Canedoli C, Manenti R, Padoa-Schioppa E (2018) Birds biodiversity in urban and periurban forests: environmental determinants at local and landscape scales. Urban Ecosyst 21:779–793. https://doi.org/10.1007/s11252-018-0757-7

Cao X, Onishi A, Chen J, Imura H (2010) Quantifying the cool island

intensity of urban parks using ASTER and IKONOS data. Landsc Urban Plan 96:224–231. https://doi.org/10.1016/j.landurbplan.2010.03.008

Carneiro C, Morello E, Desthieux G (2009) Assessment of Solar Irradiance on the Urban Fabric for the Production of Renewable Energy using LIDAR Data and Image Processing Techniques. Lect. Notes Geoinf. Cartogr. 83–112

Charreire H, Mackenbach JD, Ouasti M, et al (2014) Using remote sensing to define environmental characteristics related to physical activity and dietary behaviours: A systematic review (the SPOTLIGHT project). Heal Place 25:1–9. https://doi.org/10.1016/j.healthplace.2013.09.017

Chen Z, Devereux B, Gao B, Amable G (2012) Upward-fusion urban DTM generating method using airborne Lidar data. ISPRS J Photogramm Remote Sens 72:121–130. https://doi.org/10.1016/j.isprsjprs.2012.07.001

Chen Z, Xu B, Devereux B (2014) Urban landscape pattern analysis based on 3D landscape models. Appl Geogr 55:82–91. https://doi.org/10.1016/j.apgeog.2014.09.006

Chun B, Guldmann JM (2018) Impact of greening on the urban heat island: Seasonal variations and mitigation strategies. Comput Environ Urban Syst 71:165–176. https://doi.org/10.1016/j.compenvurbsys.2018.05.006

Côté JF, Fournier RA, Egli R (2011) An architectural model of trees to estimate forest structural attributes using terrestrial LiDAR. Environ

Model Softw 26:761–777.
https://doi.org/10.1016/j.envsoft.2010.12.008

Dassot M, Constant T, Fournier M (2011) The use of terrestrial LiDAR technology in forest science: Application fields, benefits and challenges. Ann For Sci 68:959–974. https://doi.org/10.1007/s13595-011-0102-2

Fan Y, Feng Z, Mannan A, et al (2018) Estimating Tree Position, Diameter at Breast Height, and Tree Height in Real-Time Using a Mobile Phone with RGB-D SLAM. Remote Sens 10:1845. https://doi.org/10.3390/rs10111845

Fitzpatrick K, Carlson P, Brewer M, Wooldridge M (2001) Design Factors That Affect Driver Speed on Suburban Streets. Transp Res Rec 18–25. https://doi.org/10.3141/1751-03

Geiß C, Taubenböck H, Wurm M, et al (2011) Remote sensing-based characterization of settlement structures for assessing local potential of district heat. Remote Sens 3:1447–1471. https://doi.org/10.3390/rs3071447

Gong FY, Zeng ZC, Ng E, Norford LK (2019) Spatiotemporal patterns of street-level solar radiation estimated using Google Street View in a high-density urban environment. Build Environ 148:547–566. https://doi.org/10.1016/j.buildenv.2018.10.025

Gong FY, Zeng ZC, Zhang F, et al (2018) Mapping sky, tree, and building view factors of street canyons in a high-density urban environment. Build Environ 134:155–167.

https://doi.org/10.1016/j.buildenv.2018.02.042

Grau E, Durrieu S, Fournier R, et al (2017) Estimation of 3D vegetation density with Terrestrial Laser Scanning data using voxels. A sensitivity analysis of influencing parameters. Remote Sens Environ 191:373–388. https://doi.org/10.1016/j.rse.2017.01.032

Hämmerle M, Gál T, Unger J, Matzarakis A (2011) Introducing a script for calculating the sky view factor used for urban climate investigations. Acta Climatol Chorol 44–45:83–92

Hatefnia N, Barakati A, Ghobad M, Eslam Panah A (2017) Unified evaluation of total radiation in urban environments. Archit Sci Rev 60:266–274. https://doi.org/10.1080/00038628.2017.1336980

Heo HK, Lee DK, Park JH, Thorne JH (2019) Estimating the heights and diameters at breast height of trees in an urban park and along a street using mobile LiDAR. Landsc Ecol Eng 15:. https://doi.org/10.1007/s11355-019-00379-6

Holmer B, Postgård U, Ericksson M (2001) Sky view factors in forest canopies calculated with IDRISI. Theor Appl Climatol 68:33–40. https://doi.org/10.1007/s007040170051

Hopkinson C, Chasmer L, Young-Pow C, Treitz P (2004) Assessing forest metrics with a ground-based scanning lidar. Can J For Res 34:573–583. https://doi.org/10.1139/x03-225

Hosoi F, Omasa K (2009) Estimating Vertical Leaf Area Density Profiles of Tree Canopies Using Three-Dimensional Portable Lidar Imaging. XXXVIII:152–157

Huang H, Li Z, Gong P, et al (2011) Automated Methods for Measuring DBH and Tree Heights with a Commercial Scanning Lidar. Photogramm Eng Remote Sens 77:219–227. https://doi.org/10.14358/PERS.77.3.219

Jiang B, Li D, Larsen L, Sullivan WC (2014) A Dose-Response Curve Describing the Relationship Between Urban Tree Cover Density and Self-Reported Stress Recovery. Environ Behav 48:607–629. https://doi.org/10.1177/0013916514552321

Jiang B, Sullivan WC, Chang C-Y, et al (2016) Remotely-sensed imagery vs. eye-level photography: Evaluating associations among measurements of tree cover density. Landsc Urban Plan 157:270–281. https://doi.org/10.1016/j.landurbplan.2016.07.010

Jo H-K, Ahn T-W (2012) Carbon Storage and Uptake by Deciduous Tree Species for Urban Landscape. J Korean Inst Landsc Archit 40:160–168. https://doi.org/10.9715/KILA.2012.40.5.160

Jo H, Kim J, Park H (2013) Carbon Storage and Uptake by Evergreen Trees for Urban Landscape - For Pinus densiflora and Pinus koraiensis -. Korean J Environ Ecol 27:571–578. https://doi.org/10.13047/KJEE.2013.27.5.571

Jung SE, Kwak DA, Park T, et al (2011) Estimating crown variables of individual trees using airborne and terrestrial laser scanners. Remote Sens 3:2346–2363. https://doi.org/10.3390/rs3112346

Kidd C, Chapman L (2012) Derivation of sky-view factors from lidar data. Int J Remote Sens 33:3640–3652.

https://doi.org/10.1080/01431161.2011.635163

Kim JH, Gu D, Sohn W, et al (2016a) Neighborhood landscape spatial patterns and land surface temperature: An empirical study on single-family residential areas in Austin, Texas. Int J Environ Res Public Health 13:. https://doi.org/10.3390/ijerph13090880

Kim JH, Lee C, Sohn W (2016b) Urban natural environments, obesity, and health-related quality of life among hispanic children living in Inner-City neighborhoods. Int J Environ Res Public Health 13:. https://doi.org/10.3390/ijerph13010121

Korhonen L, Vauhkonen J, Virolainen A, et al (2013) Estimation of tree crown volume from airborne lidar data using computational geometry. Int J Remote Sens 34:7236–7248. https://doi.org/10.1080/01431161.2013.817715

Lee K, Levermore GJ (2019) Sky view factor and sunshine factor of urban geometry for urban heat island and renewable energy. Archit Sci Rev 62:26–34. https://doi.org/10.1080/00038628.2018.1536601

Li F, Song G, Liujun Z, et al (2017) Urban vegetation phenology analysis using high spatio-temporal NDVI time series. Urban For Urban Green 25:43–57. https://doi.org/10.1016/j.ufug.2017.05.001

Li X, Zhang C, Li W, et al (2015a) Who lives in greener neighborhoods? The distribution of street greenery and its association with residents' socioeconomic conditions in Hartford, Connecticut, USA. Urban For Urban Green 14:751–759. https://doi.org/10.1016/j.ufug.2015.07.006

Li X, Zhang C, Li W, et al (2015b) Assessing street-level urban greenery

using Google Street View and a modified green view index. Urban For Urban Green 14:675–685. https://doi.org/10.1016/j.ufug.2015.06.006

Li X, Zhang C, Li W, Kuzovkina YA (2016) Environmental inequities in terms of different types of urban greenery in Hartford, Connecticut. Urban For Urban Green 18:163–172. https://doi.org/10.1016/j.ufug.2016.06.002

Lindberg F, Grimmond C (2011) The influence of vegetation and building morphology on shadow patterns and mean radiant temperatures in urban areas : model development and evaluation . Theor Appl Climatol on shadow patterns and mean radiant temperatures. Theor Appl Climatol · 311–323. https://doi.org/10.1007/s00704-010-0382-8

Lindberg F, Holmer B, Thorsson S (2008) SOLWEIG 1.0 - Modelling spatial variations of 3D radiant fluxes and mean radiant temperature in complex urban settings. Int. J. Biometeorol. 52:697–713

Liu L, Silva EA, Wu C, Wang H (2017) A machine learning-based method for the large-scale evaluation of the qualities of the urban environment. Comput Environ Urban Syst 65:113–125. https://doi.org/10.1016/j.compenvurbsys.2017.06.003

Lu Y (2018) Using Google Street View to investigate the association between street greenery and physical activity. Landsc Urban Plan. https://doi.org/10.1016/j.landurbplan.2018.08.029

Lu Y, Yang Y, Sun G, Gou Z (2019) Associations between overhead-view and eye-level urban greenness and cycling behaviors. Cities 88:10–18. https://doi.org/10.1016/j.cities.2019.01.003

Luo L, Zhai Q, Su Y, et al (2018) Simple method for direct crown base height estimation of individual conifer trees using airborne LiDAR data. Opt Express 26:A562. https://doi.org/10.1364/oe.26.00a562

Martínez-Rubio A, Sanz-Adan F, Santamaría-Peña J, Martínez A (2016) Evaluating solar irradiance over facades in high building cities, based on LiDAR technology. Appl Energy 183:133–147. https://doi.org/10.1016/j.apenergy.2016.08.163

Næsset E, Økland T (2002) Estimating tree height and tree crown properties using airborne scanning laser in a boreal nature reserve. Remote Sens Environ 79:105–115. https://doi.org/10.1016/S0034-4257(01)00243-7

Nielsen AB, van den Bosch M, Maruthaveeran S, van den Bosch CK (2013) Species richness in urban parks and its drivers: A review of empirical evidence. Urban Ecosyst 17:305–327. https://doi.org/10.1007/s11252-013-0316-1

Nordh H, Hartig T, Hagerhall CM, Fry G (2009) Components of small urban parks that predict the possibility for restoration. Urban For Urban Green 8:225–235. https://doi.org/10.1016/j.ufug.2009.06.003

Nowak DJ, Crane DE (2002) Carbon storage and sequestration by urban trees in the USA. Environ Pollut 116:381–389. https://doi.org/10.1016/S0269-7491(01)00214-7

Nowak DJ, Stein SM, Randler PB, et al (2010) Sustainning America's Urban Trees and Forests: a Forests on the Edge report. 28

Odgers CL, Caspi A, Bates CJ, et al (2012) Systematic social observation of children's neighborhoods using Google Street View: A reliable and

cost-effective method. J Child Psychol Psychiatry Allied Discip
53:1009–1017. https://doi.org/10.1111/j.1469-7610.2012.02565.x

Olofsson K, Holmgren J, Olsson H (2014) Tree stem and height
measurements using terrestrial laser scanning and the RANSAC
algorithm. Remote Sens 6:4323–4344.
https://doi.org/10.3390/rs6054323

Oshio H, Asawa T, Hoyano A, Miyasaka S (2015) Estimation of the leaf
area density distribution of individual trees using high-resolution and
multi-return airborne LiDAR data. Remote Sens Environ 166:116–125.
https://doi.org/10.1016/j.rse.2015.05.001

Pagani-Núñez E, He C, Wu YW, et al (2017) Foraging in the tropics:
relationships among species' abundances, niche asymmetries and body
condition in an urban avian assemblage. Urban Ecosyst 20:1301–1310.
https://doi.org/10.1007/s11252-017-0682-1

Park J, Kim JH, Lee DK, et al (2017) The influence of small green space
type and structure at the street level on urban heat island mitigation.
Urban For Urban Green 21:203–212.
https://doi.org/10.1016/j.ufug.2016.12.005

Pierzchała M, Giguère P, Astrup R (2018) Mapping forests using an
unmanned ground vehicle with 3D LiDAR and graph-SLAM. Comput
Electron Agric 145:217–225.
https://doi.org/10.1016/j.compag.2017.12.034

Popescu SC, Zhao K (2008) A voxel-based lidar method for estimating
crown base height for deciduous and pine trees. Remote Sens Environ

112:767–781. https://doi.org/10.1016/j.rse.2007.06.011

Pratt V (1987) Direct least-squares fitting of algebraic surfaces. ACM
SIGGRAPH Comput Graph 21:145–152.
https://doi.org/10.1145/37402.37420

Ren Z, He X, Zheng H, et al (2013) Estimation of the relationship between
urban park characteristics and park cool island intensity by remote
sensing data and field measurement. Forests 4:868–886.
https://doi.org/10.3390/f4040868

Robitu M, Musy M, Inard C, Groleau D (2006) Modeling the influence of
vegetation and water pond on urban microclimate. Sol Energy 80:435–
447. https://doi.org/10.1016/j.solener.2005.06.015

Seo YO, Lumbres RIC, Won HK, et al (2015) Evaluation and validation of
stem volume models for quercus glauca in the subtropical forest of jeju
island, korea. J Ecol Environ 38:485–491.
https://doi.org/10.5141/ecoenv.2015.051

Song C (2013) Optical remote sensing of forest leaf area index and biomass.
Prog Phys Geogr 37:98–113.
https://doi.org/10.1177/0309133312471367

Song Y, Imanishi J, Sasaki T, et al (2016) Estimation of broad-leaved
canopy growth in the urban forested area using multi-temporal airborne
LiDAR datasets. Urban For Urban Green 16:142–149.
https://doi.org/10.1016/j.ufug.2016.02.007

Song Y, Ryu Y (2015) Seasonal changes in vertical canopy structure in a
temperate broadleaved forest in Korea. Ecol Res 30:821–831.

https://doi.org/10.1007/s11284-015-1281-3

Souza LCL, Rodrigues DS, Mendes JFG (2003) SKY VIEW FACTORS
ESTIMATION USING A 3D-GIS EXTENSION São Paulo State
University , Bauru , Brazil University of Minho , Braga , Portugal.
Simulation 1227–1234

Storbeck J, Clore GL, Storbeck J, Clore GL (2017) On the interdependence
of cognition and emotion. 9931:.
https://doi.org/10.1080/02699930701438020

Susaki J, Komiya Y, Takahashi K (2014) Calculation of enclosure index for
assessing urban landscapes using digital surface models. IEEE J Sel
Top Appl Earth Obs Remote Sens 7:4038–4045.
https://doi.org/10.1109/JSTARS.2013.2271380

Susaki J, Kubota S (2017) Automatic assessment of green space ratio in
urban areas from mobile scanning data. Remote Sens 9:.
https://doi.org/10.3390/rs9030215

Suzuki R, Nomaki T, Yasunari T (2001) Spatial distribution and its
seasonality of satellite-derived vegetation index (NDVI) and climate in
Siberia. Int J Climatol 21:1321–1335. https://doi.org/10.1002/joc.653

Svensson MK (2004) Sky view factor analysis – implications for urban air
temperature differences. Meteorol. Appl 11:201–211

Tan PY, Wang J, Sia A (2013) Perspectives on five decades of the urban
greening of Singapore. Cities 32:24–32.
https://doi.org/10.1016/j.cities.2013.02.001

Teller BJ, Miller AD, Shea K (2014) Conservation of passively dispersed

organisms in the context of habitat degradation and destruction. J Appl Ecol n/a-n/a. https://doi.org/10.1111/1365-2664.12379

Teller J, Azar S (2001) Townscope II - A computer systems to support solar access decision-making. Sol Energy 70:187–200. https://doi.org/10.1016/S0038-092X(00)00097-9

Unger J (2009) Connection between urban heat island and sky view factor approximated by a software tool on a 3D urban database. Int J Environ Pollut 36:59–80

Vanwolleghem G, Van Dyck D, Ducheyne F, et al (2014) Assessing the environmental characteristics of cycling routes to school: A study on the reliability and validity of a Google Street View-based audit. Int J Health Geogr 13:1–9. https://doi.org/10.1186/1476-072X-13-19

Wang J, Cheng Q, Chen J (2011) A GIS and remote sensing-based analysis of land use change using the asymmetric relation analysis method: A Case study from the City of Hangzhou, China. Math Geosci 43:435–453. https://doi.org/10.1007/s11004-011-9324-y

Wang R, Lu Y, Zhang J, et al (2019) The relationship between visual enclosure for neighbourhood street walkability and elders' mental health in China: Using street view images. J Transp Heal 13:90–102. https://doi.org/10.1016/j.jth.2019.02.009

Watson ID, Johnson GT (1987) Graphical estimation of sky view factors in urban environments. J Climatol 7:193–197. https://doi.org/10.1002/joc.3370070210

Watts K, Eycott AE, Handley P, et al (2010) Targeting and evaluating

biodiversity conservation action within fragmented landscapes: an approach based on generic focal species and least-cost networks. Landsc Ecol 25:1305–1318. https://doi.org/10.1007/s10980-010-9507-9

Wey WM, Wei WL (2016) Urban Street Environment Design for Quality of Urban Life. Soc Indic Res 126:161–186. https://doi.org/10.1007/s11205-015-0880-2

Xu Y, Ren C, Ma P, et al (2017) Urban morphology detection and computation for urban climate research. Landsc Urban Plan 167:212–224. https://doi.org/10.1016/j.landurbplan.2017.06.018

Yang J, Zhao L, Mcbride J, Gong P (2009) Can you see green? Assessing the visibility of urban forests in cities. Landsc Urban Plan 91:97–104. https://doi.org/10.1016/j.landurbplan.2008.12.004

Yang L, Sheng Y, Wang B (2016) 3D reconstruction of building facade with fused data of terrestrial LiDAR data and optical image. Optik (Stuttg) 127:2165–2168. https://doi.org/10.1016/j.ijleo.2015.11.147

Yao T, Yang X, Zhao F, et al (2011) Measuring forest structure and biomass in New England forest stands using Echidna ground-based lidar. Remote Sens Environ 115:2965–2974. https://doi.org/10.1016/j.rse.2010.03.019

Ye Y, Richards D, Lu Y, et al (2018) Measuring daily accessed street greenery: A human-scale approach for informing better urban planning practices. Landsc Urban Plan. https://doi.org/10.1016/j.landurbplan.2018.08.028

Yi YK, Kim H (2017) Universal Visible Sky Factor: A method for calculating the three-dimensional visible sky ratio. Build Environ 123:390–403. https://doi.org/10.1016/j.buildenv.2017.06.044

Yin L, Cheng Q, Wang Z, Shao Z (2015) "Big data" for pedestrian volume: Exploring the use of Google Street View images for pedestrian counts. Appl Geogr 63:337–345. https://doi.org/10.1016/j.apgeog.2015.07.010

Yin L, Wang Z (2016) Measuring visual enclosure for street walkability: Using machine learning algorithms and Google Street View imagery. Appl Geogr 76:147–153. https://doi.org/10.1016/j.apgeog.2016.09.024

Yoon TK, Park CW, Lee SJ, et al (2013) Allometric equations for estimating the aboveground volume of five common urban street tree species in Daegu, Korea. Urban For Urban Green 12:344–349. https://doi.org/10.1016/j.ufug.2013.03.006

Yu S, Yu B, Song W, et al (2016) View-based greenery: A three-dimensional assessment of city buildings' green visibility using Floor Green View Index. Landsc Urban Plan 152:13–26. https://doi.org/10.1016/j.landurbplan.2016.04.004

Yu X, Zhao G, Chang C, et al (2018) BGVI: A new index to estimate street-side greenery using Baidu Street View Image. Forests 10:1–13. https://doi.org/10.3390/f10010003

Yuan Y, Zeng G, Liang J, et al (2014) Effects of landscape structure, habitat and human disturbance on birds: A case study in East Dongting Lake wetland. Ecol Eng 67:67–75. https://doi.org/10.1016/j.ecoleng.2014.03.012

Zhang J, Heng CK, Malone-Lee LC, et al (2012) Evaluating environmental implications of density: A comparative case study on the relationship between density, urban block typology and sky exposure. Autom Constr 22:90–101. https://doi.org/10.1016/j.autcon.2011.06.011

Zhang Y, Dong R (2018) Impacts of Street-Visible Greenery on Housing Prices: Evidence from a Hedonic Price Model and a Massive Street View Image Dataset in Beijing. ISPRS Int J Geo-Information 7:104. https://doi.org/10.3390/ijgi7030104

Zhang Y, Middel A, Turner BL (2019) Evaluating the effect of 3D urban form on neighborhood land surface temperature using Google Street View and geographically weighted regression. Landsc Ecol 34:681–697. https://doi.org/10.1007/s10980-019-00794-y

Zhao Y, Hu Q, Li H, et al (2018) Evaluating Carbon Sequestration and PM2.5 Removal of Urban Street Trees Using Mobile Laser Scanning Data. Remote Sens 10:1759. https://doi.org/10.3390/rs10111759
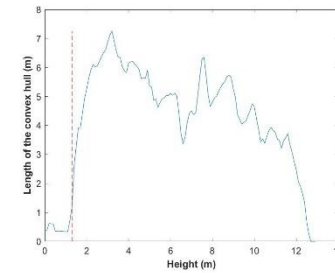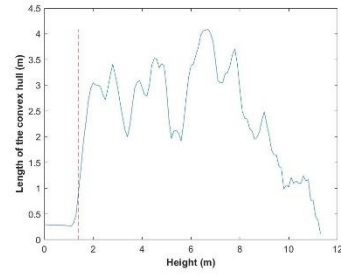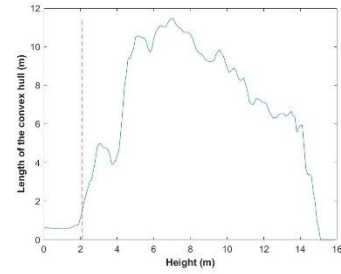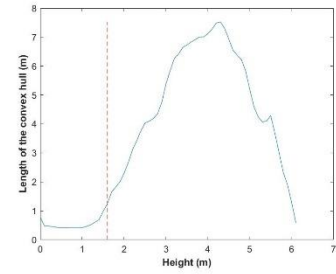
VIII. Appendix
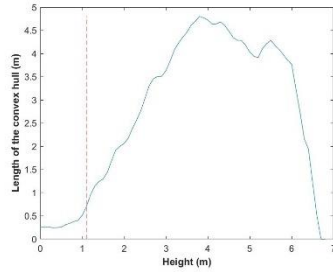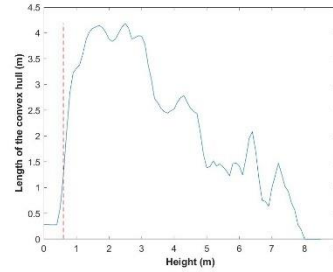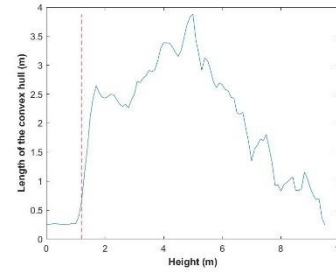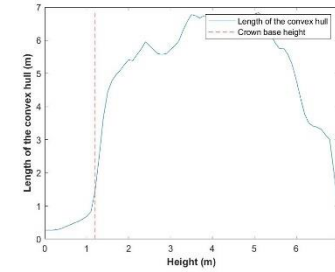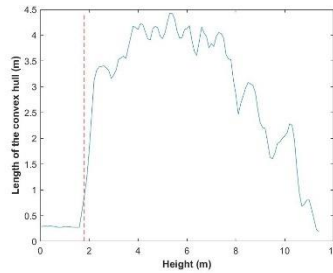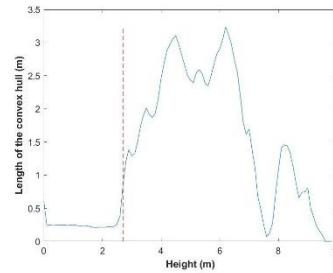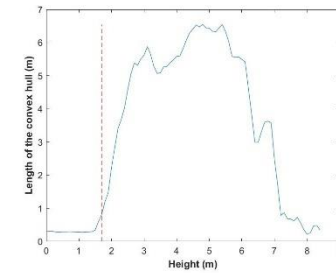
Appendix 1. Length of the convex hull at each height (r1-r8).
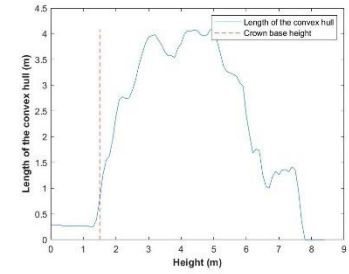
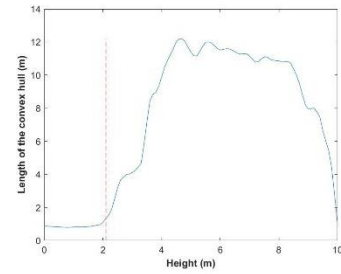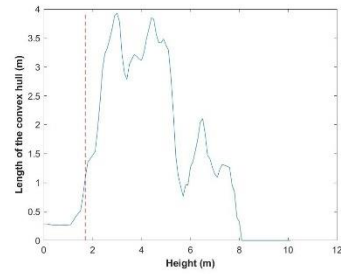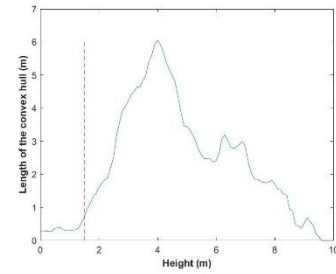**Appendix 2.** Length of the convex hull at each height (r9-r15).

국문 초록

지상 라이다를 이용한 도시 가로
천공률과 녹시율 평가

허 한 결

서울대학교 대학원
협동과정 조경학
지도교수: 이 동 근

도시 가로 환경은 생물 다양성을 증진, 탄소를 저장, 도시열섬 효과를 완화, 도시 주민의 신체적, 정신적 건강 증진 등 다양한 기능을 수행한다. 이에 따라 도시 가로 환경 구조를 정량화 하기 위한 연구가 진행되어왔다. 특히 최근에는 LiDAR (Light Detection and Ranging) 시스템의 개발로 3차원 데이터 수집이 가능해졌고, 이로 인해 도시 구조의 정확한 측정이 가능해졌다. 이에 따라 기존 2차원 데이터의 한계로 직접 대상지에서 사진촬영을 통해 구축되던 천공률과 녹시율 등의 데이터 구축이 가능해졌다.

녹시율 분석을 위해 수목의 수관을 분류하는 등 LiDAR데이터의 전처리 과정이 필요하다. 특히 나무는 도시 가로 환경에서 가장 중요한 생태 요소이며, 수목 데이터의 정량화는 LiDAR데이터를 이용한 분석에서 중요한 기초자료가 된다. 이에 본 연구에서는 첫 번째로, mobile LiDAR을 사용하여 도시 수목의 수고, 지하고, 흉고직경을 분석하고 정확도를 검증하였다. 결과적으로 수고와 지하고는 각각 RMSE가 0.359m와 0.09m로 나타나 높은 정확도를 나타내었다. 반면 흉고직경은 RMSE 0.0377m로 중간 정도의 정확도를 나타냈다.

　　본 연구에서 두 번째로 분석한 천공률은 도시 인프라와 관련된 주요 지표이며 도시 열섬 및 재생 가능 에너지 연구에서 태양복사에너지양을 산정하기 위해 주로 사용된다. 그러나 기존 방법은 정확도 측면에서 한계가 있거나, 현장조사를 통해 데이터를 구축하여 한계가 있었다. 최근 LiDAR를 사용하여 복잡한 도시 지역에서도 천공률 계산이 가능해졌다. 그러나 항공 LiDAR의 해상도 한계로 인해 나무가 있는 도시지역에서의 정확도가 떨어졌다. 따라서 본 연구는 지상 LiDAR을 이용한 천공률 계산의 정확성을 검

증하고자 하였으며, 항공 LiDAR보다 높은 정확도로 천공률을 계산하였다. 지상 LiDAR 기반 SVF의 결과는 R^2 0.915, RMSE 0.037, 최대 오차 0.156으로 높은 정확도를 나타냈다. 본 연구에 따르면 지상 LiDAR의 경우 복셀 크기 2.5cm가 복잡한 도시 지역에서 SVF를 추정하기에 적합하며, 항공 LiDAR과 비교하여 최대 오차를 60 % 감소시킬 수 있는 것으로 나타났다.

마지막으로 본 연구에서는 천공률과 녹시율 데이터의 도시 규모 구축 가능성에 대해 분석하고 구축 방법을 제시하였다. 연구 결과에 따르면 LiDAR 데이터의 해상도가 높을수록 결과의 정확도가 높아진다. 그러나 높은 해상도의 LiDAR 데이터로 높은 해상도의 데이터를 구축하기 위해서는 분석량이 많아 시간 효율이 떨어진다. 이에 대해 본 연구에서는 가상의 복셀화된 3차원 환경에서 시뮬레이션 분석을 수행하여 효율적인 데이터 구축 방법을 도출하고자 하였다. 연구 결과에 따르면 도로 위 어떤 차선에서 분석하는지에 따라 천공률과 녹시율 값의 변동이 크게 나타나며, 도로의 폭에 따라 연구 대상지를 대표할 수 있는 위치를 특정지을 수 있음을 도출하였다. 천공률과 녹시율 모두 대상지의 평균과 가장 가

까운 위치가 도로 폭에 따라 왕복 8차선 도로에서는 3차선, 왕복 6차선 도로에서는 2차선에서 나타나며, 왕복 4차선과 2차선에서는 각각 2차선과 1차선에서 나타난다. 따라서 연구 대상지 모든 지점에서 분석하지 않고 도출된 지점에서 분석한다면 연구 대상지를 대표하는 천공률과 녹시율을 쉽게 도출할 수 있다.

본 연구를 통해 LiDAR 데이터를 이용한 가로환경 중 천공률과 녹시율 데이터 구축을 더 효율적으로 할 수 있을 것으로 기대된다. 이는 기존 사진촬영을 통해 높은 정확도의 데이터를 낮은 효율로 취득하는 방식이나 2차원, 2.5차원 데이터를 통해 중간 정확도의 데이터를 높은 효율로 취득하는 방식에 비해 상당부분 개선된 것으로 판단된다. 또한 LiDAR 데이터를 이용함에 있어서도 분석 효율을 높여, 넓은 대상지에서도 결과물을 도출하는 시간을 앞당길 수 있을 것으로 기대할 수 있다.